Plasma Chemistry and Plasma Processing (2025) 45:1849–1899
https://doi.org/10.1007/s11090-025-10599-4

ORIGINAL PAPER

How Plasma Reaction Conditions Affect the Optimal Catalyst: A Microkinetic Study of Plasma-catalytic CO_2 Splitting

Björn Loenders[1,2] · Roel Michiels[1,2] · Annemie Bogaerts[1,2]

Received: 5 April 2025 / Accepted: 9 September 2025 / Published online: 23 September 2025

Abstract

Plasma catalysis is promising for greenhouse gas conversion into value-added chemicals, yet this technology is still poorly understood due to the complexity of the underlying mechanisms. Therefore, we study the chemical kinetic effects of the interaction between plasma species and glass or transition metal (Ag, Cu, Pd and Rh) surfaces placed in the afterglow of a low-pressure CO_2 plasma. We developed a coupled plasma-surface model to study how different catalyst surfaces and reaction conditions (i.e., temperature, pressure and flow rate) affect the spatial evolution of the O_2 and CO mole fractions for plasma-catalytic CO_2 splitting. Moreover, we used density functional theory (DFT) to determine the reaction barriers on the metal surfaces and used these as input for our kinetic model. Although our model could not yet be validated against experimental data, it can provide qualitative trends, insights and comparisons on the influence of the different catalysts and reactions conditions. Firstly, our results indicate that Eley-Rideal (E-R), or more correctly Langmuir-Rideal (L-R), reactions play an essential role in the recombination of O atoms into O_2. Secondly, we find that the optimal catalyst depends strongly on the reactions conditions. For example, Cu performs very well at low and intermediate temperatures (500–1000 K) for which Ag performs poorly, while Ag yields the highest maximum O_2 fractions at higher temperatures (>1000 K), and thus the least recombination between O and CO back to CO_2. Pd was found to be detrimental to CO_2 splitting, as it catalyzes the oxidation of CO, while Rh is relatively inactive for both O_2 formation and thermal catalytic CO oxidation under most conditions. Thus, the optimal catalyst depends both on its activity for O atom recombination into O_2, as well as for thermal catalytic CO oxidation to form CO_2. Moreover, if the catalyst is active for thermal catalytic CO oxidation, this back-reaction should be avoided by optimizing the flow rate or the length of the catalytic bed. Hence, this study illustrates how trends between different catalysts for plasma catalysis can change depending on the reaction conditions, which is important to consider when comparing different catalysts experimentally.

✉ Björn Loenders
bjorn.loenders@uantwerpen.be

[1] Research group PLASMANT, Department of Chemistry, University of Antwerp, Universiteitsplein 1, Wilrijk-Antwerp B-2610, Belgium

[2] Electrification Institute, University of Antwerp, Olieweg 97, Antwerp 2020, Belgium

Introduction

In the last decades there is a growing awareness for the need to lower the amount of anthropogenic greenhouse gas (GHG) emissions, as global warming and the resulting climate change are an increasing problem [1]. One way of reducing GHG emissions into the atmosphere is through carbon capture and utilization (CCU), in which CO_2 is captured and used as a feedstock for the production of value-added carbon-containing products [2]. Plasma technology is a promising method for the conversion of CO_2 into value-added chemicals and fuels [3]. This method involves the creation of electrical discharges in which energy is transferred to the gas molecules by highly energetic electrons, rather than by conventional heating. As such, plasma technology enables the activation of highly thermodynamically stable molecules, such as CO_2, at relatively mild temperatures. Moreover, as this process is powered by electricity and can rapidly be switched on and off, it can make use of renewable energy, such as from wind or solar power [3].

However, collisions between electrons and gas molecules result in various reactive plasma species, which can form a broad range of products. Plasma catalysis therefore combines plasma with a catalyst to improve the reactant conversion and selectivity towards targeted products. Ideally, synergy between the plasma and catalyst is attained, meaning that the conversion or product yield of plasma catalysis surpasses the sum of the conversions or yields of the plasma and catalyst alone [4]. Yet, the conditions that lead to plasma-catalyst synergy are usually not known a priori, and experimentally they have to be identified in practice through trial-and-error. Indeed, a thorough and fundamental understanding of the mechanisms responsible for synergy is still lacking, due to the highly complex nature of plasma catalysis [5, 6].

Plasma catalysis is most often executed by directly placing a catalyst material inside the plasma reactor, typically in a packed-bed (so-called in-plasma catalysis). This is only possible in non-thermal plasmas, such as dielectric barrier discharges (DBDs), as these operate at sufficiently low temperatures (300–1000 K). Indeed, warm plasmas, like microwave (MW) and gliding arc (GA) discharges, cannot be used in this configuration as their high temperatures (typically multiple 1000 K) would result in destruction of the catalyst [4, 6].

The use of a packed-bed DBD configuration results in a variety of physical and chemical interactions between the plasma and the catalyst (or packing material). For example, introduction of a packing in the discharge gap can alter the discharge type (i.e., localized vs. surface discharges) by locally enhancing the electric field due to the presence of (catalyst) nanostructures or polarization of the dielectric packing material. While the plasma properties are affected by the catalyst, this is also true the other way around, e.g., reactive plasma species, such as electrons, ions, radicals, and vibrationally and electronically excited molecules, can alter the catalyst surface chemistry if they reach its surface [5, 7, 8]. As the various plasma-catalyst interactions can occur simultaneously, it is difficult to study the contribution of each individual effect to the global reaction. Hence, the underlying mechanisms responsible for synergy between plasma and catalyst are still not well understood and more fundamental research on this topic is highly needed [5–7].

This fundamental research can be performed by carefully designed experiments, which should ideally be executed using standardized experiment setups, or by computational models, which can be developed to focus on specific interactions. This way, plasma-catalyst

interactions can be isolated as much as possible to study their individual effects and identify whether they contribute to plasma-catalyst synergy, and if so, under what circumstances [5].

In this regard, various authors have employed microkinetic modelling to study how reactive plasma species can affect the catalyst surface chemistry. Metha et al. [9] postulated that vibrational excitation of N_2 lowers its barrier for dissociative adsorption, and illustrated how this affects plasma-catalytic NH_3 synthesis using microkinetic modelling. The authors found that N_2 vibrational excitation enhances the turnover frequency of NH_3 on catalysts that bind N moderately to weakly, as N_2 dissociation is the rate-limiting step on these surfaces. Moreover, the optimal catalyst for NH_3 production was found to shift towards more weakly binding metals [9]. In a follow-up study, Metha et al. [10] showed that N_2 vibrational excitation can enhance the NH_3 concentration to values exceeding the thermodynamical equilibrium for catalysts on which N_2 dissociation is rate-limiting. Moreover, the departure from equilibrium was found to be larger for metals that bind N more weakly, i.e., as these are more strongly limited by N_2 dissociation and thus result in more strongly enhanced forward reaction rates. However, at high temperatures, the reverse reactions, that cause NH_3 destruction, become thermally active, hence causing the NH_3 concentrations to return to the equilibrium values [10].

Engelmann et al. [11] used microkinetic modelling to study the effects of both vibrationally excited CH_4 and plasma-produced radicals on the non-oxidative coupling of CH_4. They found that vibrational excitation was most beneficial on intermediately binding catalysts, which remained near the top of the volcano curve. Additionally, a shift in product selectivity occurred, with C_2H_4 becoming favored over C_2H_2 on these catalysts. This was due to vibrational excitation only enhancing CH_4 dissociation, but not the subsequent dehydrogenation steps. Contrary to vibrationally excited CH_4, the presence of radicals resulted in the highest turnover frequencies on the most weakly binding metals, as CH_4 dissociative adsorption, which is strongly rate-limiting for these catalysts, was completely omitted [11]. In another study, Engelmann et al.[12] compared the effect of vibrationally excited N_2 and plasma radicals on the surface chemistry for plasma-catalytic NH_3 synthesis, and investigated the potential effect of Eley-Rideal (E-R) reactions, i.e., between impinging gas species and adsorbates. Note that the correct name for this type of reaction should be Langmuir-Rideal (L-R) reaction, as Langmuir was the first to describe this mechanism,[13] so we will use it from now on. Engelmann et al. [12] found that the shift of the volcano maximum towards more weakly binding metals and the rise of the turnover frequencies on these catalysts were overshadowed by the effect of plasma radicals. When only Langmuir-Hinshelwood (L-H) reactions between surface adsorbates were allowed, the presence of radicals strongly enhanced the NH_3 turnover frequencies on the most weakly binding catalysts. However, when L-R reactions between an incoming radical and an adsorbate were included, this led to universally high turnover frequencies on all metals. Yet, this conclusion was found to be only valid if the activation enthalpies of the L-R reactions were (close to) zero [12].

Michiels et al.[14] investigated how radicals, stable intermediates and vibrationally excited CO_2 molecules produced by a CO_2/H_2 plasma affect the surface pathways and kinetics of CH_3OH production on Cu(111). Although vibrationally excited CO_2 improved the CH_3OH turnover frequencies, the effect of radicals and stable intermediates was found to be much larger. The presence of plasma-produced CO molecules, and H and O atoms, enhanced the CH_3OH production via the formate path, by circumventing the difficult HCOO* formation directly from CO_2 [14]. In our earlier work,[15] we studied the effect of

vibrationally excited CH_4 and O_2, as well as radicals and stable intermediates, on the partial oxidation of CH_4 over a Pt(111) surface. In agreement with other studies, we found that both vibrational excitation and radicals enhance the turnover frequencies, but that the effect of radicals clearly dominates. By varying the number densities of different species independently, we could pinpoint their influence on the reaction pathways of the various products. Our results showed that strongly dehydrogenated carbonaceous species resulted in surface coking, while O atoms counteract coking but cause overoxidation to CO_2. Hence, both types of plasma species should be balanced against each other. H radicals, as well as CH_3O and CH_3OO, were found to be essential for oxygenate production. However, we found that high radical partial pressures in general cause surface poisoning, thus limiting the potential of the plasma-catalyst interactions [15].

Ma et al.[16] developed a microkinetic model for plasma-catalytic N_2 oxidation on Pt(211) and Au(211), and compared the performance of these catalysts against each other and the plasma alone. Pt was found to benefit more from vibrationally excited molecules than Au, while Au outperforms Pt at low temperatures if high amounts of radicals are present. This is due to Pt being more strongly binding than Au. As such, Pt can break the reactant bonds more easily than Au and does not require full dissociation in the plasma. On the other hand, Au can desorb the NO molecules more easily, even at low temperature. Additionally, while high radical densities were found to be beneficial in the presence of a catalyst, this was not the case for the plasma alone, due to the reverse Zeldovich reactions between the radicals and the formed NO.[16] In a follow-up study, Ma et al.[17] compared simulations for a Pt catalyst to experimental results obtained by placing a Pt-film in the afterglow of a radio-frequency (RF) plasma. This way, complex physical interactions, such as those present in a DBD reactor, could be avoided to focus on the chemical effects. Using this approach, the authors demonstrated various degrees of freedom for optimization, such as the effect of the O_2 content in the gas mixture. The ideal O_2 content was found to be relatively low (around 10^{-3}), demonstrating the susceptibility of Pt for O* poisoning.[17] This reaction setup was also studied by Eshtehardi et al.[18], who developed a one-dimensional heterogeneous catalysis model with axial dispersion (i.e., back-mixing and diffusion in the axial direction). The authors found that back-mixing causes a drop in NO concentration at the reactor outlet and a rise in energy cost, and should thus be avoided. Changing the characteristic length of the catalyst bed was found to have little effect on the NO concentration and energy cost, except for very high values (around 2 m), for which a rise in NO concentration and a drop in energy cost were observed. Increasing the catalyst bed porosity was also found to enhance the NO concentration up to a porosity of 0.9, after which the NO concentration drops quickly as the amount of catalyst relative to the gas volume becomes too low and the contribution of surface reactions drops [18].

Maitre et al.[19] developed a coupled plasma-surface microkinetic model to study the plasma-catalytic non-oxidative coupling of CH_4 on Ni(111). The authors observed that plasma-catalyst synergy could initially be achieved, i.e., resulting in turnover frequencies that exceeded those of the plasma-only and catalyst-only cases combined. However, this synergy could only be achieved temporarily, as the surface became saturated with H*, due to dissociative adsorption of H_2 formed in the plasma. These high H* coverages were found to stimulate the back-reaction of adsorbed CH_3* to CH_4, hence inhibiting the overall reaction [19].

In our earlier work,[5] we also constructed a coupled plasma-surface microkinetic model for dry reforming of CH_4, and compared plasma catalysis with Ag, Cu or Rh (111) surfaces to a plasma without catalyst. We found that for radical-rich conditions at low temperature, such as in a DBD, the presence of weakly binding catalysts, like Ag and Cu, negatively affect the overall conversion. Due to their weakly binding character, these catalysts can easily recombine the radicals formed by dissociation of CH_4 and CO_2 in the plasma, even at low temperature. Yet, these weakly binding metals cannot catalyze further dissociation of the adsorbed plasma species, e.g., CO*, CH_3*. As such, the plasma-produced radicals and intermediates mainly recombine back to CH_4 or CO_2, or form H_2O, as these are highly thermodynamically stable products that can be readily formed from the available plasma species. The Rh catalyst, on the other hand, was largely poisoned by the radicals due to the combination of its strongly binding nature and the low reaction temperature [5]. Hence, the presence of a catalyst does not necessarily result in a beneficial effect on conversion or selectivity, as predicted by these models [5, 19] but also reported experimentally [20–24].

To summarize, weakening reactant bonds through vibrational excitation or breaking these bonds to form radicals can enhance the product turnover frequencies,[9–12, 14–17] and may even result in product concentrations that exceed the thermal equilibrium [10, 16, 17]. However, only moderately to weakly binding catalysts, on which bond dissociation is rate limiting, can benefit from this effect [9–11]. In general, the effect of plasma radicals is found to be much stronger compared to vibrational excitation,[11, 12, 14, 15] especially on the most weakly binding catalysts, as these have more difficulty with dissociating the reactants [11, 16, 17]. However, strongly binding catalysts may also benefit from the presence of plasma radicals, if the barrier for L-R reactions between the impinging radicals and surface adsorbates is sufficiently low [12]. Yet, the presence of a catalyst in the plasma is not necessarily beneficial, as the catalyst can also lower the conversion by promoting back-reactions [5, 19].

Hence, there is a need for studies that identify which combinations of reaction conditions and catalysts can achieve plasma-catalyst synergy, and which cause detrimental effects on the conversion. In this study, we therefore investigate how parameters like temperature, pressure and flow rate affect plasma-catalytic CO_2 splitting ($CO_2 \rightarrow CO + ½\ O_2$; $\Delta H° = 283$ kJ/mol)[25] and we compare these effects for different transition metal catalysts, as well as for glass, representing the wall surface for the plasma and afterglow (see below). For this purpose, we developed a new coupled plasma-surface microkinetic model, with important improvements compared to our previous work,[5] in the sense that it includes a Boltzmann solver for calculating the rates of electron impact reactions in the gas (plasma) phase. This way, we simulate the formation of plasma species in the gas phase, their subsequent interaction with the catalyst surface and the resulting change in the species densities of the gas molecules.

The system under study consists of a transition metal (Ag, Cu, Pd or Rh) or glass wall surface that surrounds the afterglow of a non-thermal plasma at low pressure (0.05-10 mbar), i.e., similar to a low-pressure RF plasma, as studied in refs. [16, 17]. This way, we avoid the complexity of DBD plasmas, which are highly inhomogeneous in both space and time and sensitive to various physical effects. Due to the absence of such physical interactions in our system, we can focus purely on the chemical effects. Moreover, our interest goes specifically towards the effect of plasma-produced radicals and ground-state molecules, as previous microkinetic models [11, 12, 14, 15] indicate that the effect of vibrationally excited molecules remains limited, when radicals are present. Note that the plasma drives CO_2

splitting into CO and O_2, and the role of the catalyst is to maximize the recombination of O atoms from the plasma into O_2 and avoid their recombination with CO back to CO_2, which would reduce the overall CO_2 conversion. Hence, the role of the plasma is to activate CO_2 to form these O atoms, as well as CO. Indeed, the thermodynamic equilibrium of the CO_2 splitting reaction is strongly shifted towards CO_2 at the conditions under study (0.5–10 mbar and 500–1100 K), for which the maximum O_2 and CO mole fractions at the thermodynamic equilibrium reach only 1×10^{-5} and 2×10^{-5}, respectively (calculated using the algorithm described in ref. 26). Therefore, the system exceeds the thermodynamic equilibrium limit for almost all cases investigated.

We do not only consider L-H reactions between adsorbed radicals, but also L-R reactions involving impinging radicals, by postulating that a correlation exists between the activation barrier of the L-R reaction and the binding strength of the involved adsorbate to the surface. Indeed, our results suggest that L-R reactions should be important in order to explain the high recombination coefficients for O atoms on transition metal surfaces that are reported in literature [27]. Moreover, our results illustrate that the optimal catalyst for plasma-catalytic CO_2 splitting is strongly dependent on the reaction conditions, especially temperature and flow rate. As such there is no "single best catalyst", and a single catalyst material can have beneficial or detrimental effects depending on reaction conditions.

Methods

Density Functional Theory Calculations

Our microkinetic model requires rate coefficients to calculate the reaction rates. For reactions on transition metal surfaces, we calculate these rate coefficients using transition state theory (TST) as will be explained in Sect. "Rate coefficients for transition metals". Because TST requires the activation barriers of the corresponding reactions, we use density functional theory (DFT) to calculate the energies and frequencies of the involved species, which are subsequently used to determine the activation barriers (see Sect. "Rate coefficients for transition metals").

To compare DFT results for different reactions and transition metal surfaces, the calculations should be performed consistently, i.e., using the same density functional, simulation settings, and ideally the same software. Some other works have studied CO oxidation with DFT for a diverse set (i.e., strongly to weakly binding) of transition metals. For example, Jiang et al.[28] used DFT to study trends between various transition metal catalysts and different surface facets, yet their work is fairly old and the size of the unit cell used in their calculations remained limited due to the computational cost at that time. More recently, Yan et al.[29] studied CO oxidation for a broad range of transition metals and their alloys. However, their focus was on the CO oxidation step, and on the CO* and O* adsorption energies, but the transition state for O_2 dissociation was not included in the DFT calculations.

To ensure a reaction set in which the DFT data for all reaction steps and transition metals is calculated consistently, we perform our own DFT calculations. Moreover, we also compute the DFT frequencies of the involved surface species, which we use to calculate their corresponding entropy, as these frequencies are often not reported in literature. All DFT

calculations are performed for the (111) facets, as the close-packed surfaces are typically the most abundant facets [30].

Table 1 lists the reactions for which the activation barriers are calculated from our DFT results. Note that dissociative adsorption is considered as a two-step reaction, i.e., adsorption of O_2 or CO_2, followed by dissociation of the molecule on the surface. Also note that the rate coefficients for L-R reactions involving gaseous O atoms are not calculated via DFT, as the transition state found along the minimum energy path does not include any dynamical effects, which are considered to be important for L-R reactions [31]. Instead, we use experimentally determined barriers, which we postulate are correlated to the O binding energy determined via DFT. Additionally, reactions on the glass surface are also described using an empirical model from literature [32–34] (see Sect. "Rate coefficients for glass surfaces"), due to the complexity associated with modelling glass surfaces via DFT.

Periodic plane-wave DFT calculations were carried out using the Vienna Ab-initio simulation Package (VASP, version 6.2.1).[35–38] The Perdew-Burke-Ernzerhof [39] functional in combination with a van der Waals functional [40] (PBE-vdW) was used. The core electrons were described by the projector augmented wave method [41, 42]. A plane-wave kinetic energy cutoff of 500 eV was used for the plane-wave basis set and the energy in the self-consistent field was converged to within 10^{-7} eV. Spin polarization was taken into account for all calculations involving O_2.

The lattice constants were optimized using a Γ-centred $20 \times 20 \times 20$ k-point mesh. The force on each atom was converged within 0.005 eV/Å. The calculated lattice constants for Ag, Cu, Pd and Rh were 4.20, 3.68, 3.99 and 3.87 Å, respectively. This is in good agreement with the experimental values of 4.08, 3.60, 3.86 and 3.83 Å, respectively [43, 44].

All metal surfaces were modelled as a 3×3 periodic 6-layer slab with a 15 Å vacuum region placed between periodically repeated slabs. During geometry optimizations, the two upper layers and adsorbates were fully relaxed, while the lower layers remained fixed at equilibrium bulk positions. A Γ-centered $8 \times 8 \times 1$ k-point mesh was used for sampling the Brillouin zone. The force on each atom was converged to within 0.01 eV/Å. The interlayer distance was optimized with these settings, where the only difference from optimizations with an adsorbate on the surface is that only the Z-coordinate is allowed to relax. The interlayer distance between the top two layers decreased with 1.9 and 0.3% for Rh and Cu, respectively. For Pd and Ag the interlayer distance increased with 0.7 and 0.5%, respectively.

Microkinetic Model

We developed a new coupled plasma-surface kinetics model, that simultaneously calculates the reaction kinetics in the gas phase (plasma and afterglow) and on the surface of the

Table 1 Reactions on the transition metal surfaces for which the activation barriers are calculated using DFT

Adsorption	Desorption
$O + * \rightarrow O*$	$O* \rightarrow O + *$
$O_2 + * \rightarrow O_2*$	$O_2* \rightarrow O_2 + *$
$CO + * \rightarrow CO*$	$CO* \rightarrow CO + *$
$CO_2 + * \rightarrow CO_2*$	$CO_2* \rightarrow CO_2 + *$
Recombination	**Dissociation**
$CO* + O* \rightarrow CO_2* + *$	$CO_2* + * \rightarrow CO* + O*$
$O* + O* \rightarrow O_2* + *$	$O_2* + * \rightarrow O* + O*$

catalyst or reactor wall. This model is a significant improvement compared to our previous model,[5] as it now includes a solver for the Boltzmann equation for electrons [45, 46]. Thus, it enables the calculation of the electron impact rate coefficients at a specified electric field or power density. The code of our model is developed in-house using Python. For the solver of the electron Boltzmann equation, we use BOLOS, an open-source Python library developed by Luque et al.[45] The model simulates the reaction kinetics inside a cylindrical reactor by treating it as multiple sequential continuously stirred tank reactor (CSTR) units, that are placed in series to approach a plug flow reactor (PFR).

Reactor Geometry and Conditions

To study the effect of plasma-created radicals on the catalytic surface pathways, we simulate a non-thermal plasma at low pressure, representative of, e.g., a low-pressure RF plasma torch [17]. Although low-pressure plasmas are not so suitable for real plasma catalysis applications, as the extra cost of pumps makes it less interesting for industrial applications, these conditions allow for relatively high radical fractions in the plasma and its afterglow, while avoiding the high computational cost and complexity associated with simulating dielectric barrier discharges (DBD's), due to their inhomogeneous nature. Additionally, we can focus on the fundamental chemical interactions between the radicals and the catalyst, without the added complexity of physical interactions (e.g., alteration of the discharge behavior) that would occur in DBD's.[4, 5, 8]

The reactor is modelled as an initial "plasma" CSTR unit, in which power is applied, followed by multiple other CSTR units in series, i.e., representing the afterglow, thus approximating a PFR. The reactor is assumed cylindrical in shape, with a radius $R = 2.0$ cm. The plasma region is modelled as a single CSTR, with a volume of 62.8 cm^3 (corresponding to a length of 5.0 cm), in which a power density of 1.59×10^6 W/m^3 is applied (corresponding to a plasma power of 100 W). The initial, "plasma" unit is followed by a region with a length of 50.0 cm in which no power is applied, to simulate the afterglow and the rest of the reactor. This zone is divided into 100 CSTR units, each with a length of 0.5 cm and a volume of 6.3 cm^3. The surface reactions and rate coefficients in the plasma region are representative for a borosilicate glass surface (see Sect. "Rate coefficients for glass surfaces"), while in the rest of the reactor, either borosilicate glass or transition metal (Ag, Cu, Pd or Rh) surfaces are used. Unless specified otherwise, the simulations are performed at a pressure of 5 mbar, and with a flow rate of 100 sccm (USA definition) [47] for pure CO_2 feed gas. One of the parameters varied is the gas (and wall) temperature, which are considered to be equal. This assumption is justified considering that heat loss of the reactor to the environment (i.e., cooling of the reactor wall) can be avoided by isolating the reactor or by placing it inside an oven. Varying the temperature between simulations allows us to study its effect on the plasma-catalyst interaction. We use temperatures in the range of 500–1100 K, considering that some heating by the plasma will be inevitable in experiments, while additional heating can be applied (e.g., by placing the reactor in an oven or preheating the feed). The typical simulation time required for the initial plasma CSTR unit is around 1–1.5 h, while the series of subsequent afterglow CSTR units solves in a couple of hours for the 100 units combined. Hence, the simulation time for the complete reactor is in the order of hours.

A schematic overview of the model is presented in Fig. 1. The model describes the reactor as a series of CSTR units (Fig. 1 (a)) with an initial 'plasma' CSTR followed by 100

smaller CSTR units describing the afterglow. The walls of the plasma CSTR are made of glass, representing a low pressure RF plasma, while the afterglow CSTRs are surrounded by a glass or catalytic metal surface. Inside a single CSTR unit, the balance of the species densities and coverages (see Sect. "Species balance equations") is described by multiple processes (Fig. 1 (b)), namely the flow of gas entering and leaving the CSTR, as well as the reactions in the bulk gas and on the surface. The different types of surface reactions included in the model are shown in Fig. 1 (c). We also provide an overview of the different reactor and operating parameters in Table 2.

Note that at the low-pressure conditions studied in this work, the (recombination) reactions in the gas phase are slow compared to the reactions on the surface. Hence, in the afterglow where $E/N = 0$, the change in density of the main gas species (CO_2, CO, O and O_2) can mostly be described based on the surface chemistry alone. However, this is not the case for the plasma stage, where electron impact reactions are important, while recombination of O+O and O+CO is still determined by the surface reactions on the glass wall. Hence, coupling the gas and surface chemistry is certainly necessary for the plasma stage. Coupling between the plasma and the post-plasma stages in the model is effectively achieved by using the output of the plasma-stage as input for the afterglow. This does also mean that if the densities in the plasma can be obtained from experiments, estimation, etc. they could in principle also be used as input for the post-plasma sections instead of the calculated values. Of course, it is still valuable to model the gas phase densities in the plasma rather than having to estimate them, especially when comparing different reaction conditions (temperature, pressure and flow rate) that affect the species densities in the plasma.

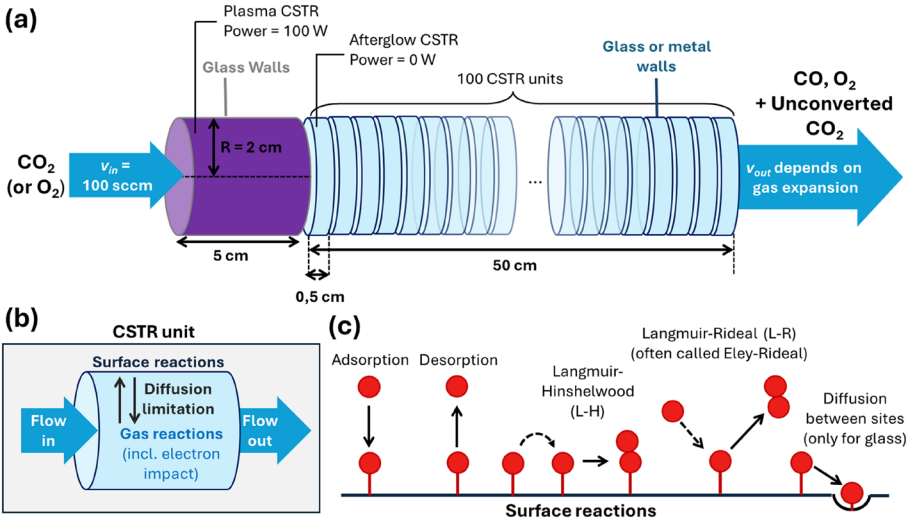

Fig. 1 Schematic representation of the model: (**a**) the reactor is modelled as a series of CSTR units, (**b**) processes governing the species densities and coverages in a single CSTR unit, (**c**) the types of surface reactions in the model

Table 2 List of the various reactor and operating parameters used in the model

Reactor radius	2 cm
Length of plasma zone	5 cm
Length of afterglow zone	50 cm
Surface/Volume ratio	100 m^{-1}
Surface site density	10^{20} m^{-2}
Sites per volume	10^{22} m^{-3}
Plasma power	100 W
Power density	1.59×10^6 W/m³
Flow rate feed	100 sccm (50–200 sccm)
Pressure	5 mbar (0.5–10 mbar)
Gas temperature	500–1100 K Constant during simulation
Wall temperature	= Gas temperature

Species Balance Equations

As discussed in Sect. "Reactor geometry and conditions" the reactor is divided into multiple consecutive units, which are modelled using a CSTR approach. This means that perfect mixing is assumed within each individual unit, hence the species densities and coverages in a single unit are uniform. However, we do consider mass transfer limitations due to diffusion to the reactor wall (see Sect. "Correction for diffusion to the wall" below). Each CSTR unit has a flow of gas entering and leaving the reactor (see Fig. 1 (b)). The gas composition of the outflow equals the composition in the CSTR volume, while the mass flow rate and composition of the feed entering the CSTR are equal to the outflow of the previous unit. Thus, the time-evolution of the species densities in a single CSTR is described using the following balance equation:

$$\frac{\partial n_s}{\partial t} = S_{rxn,\,s} + \frac{n_{s,in} v_{in}}{V_{CSTR}} - \frac{n_{s,out} v_{out}}{V_{CSTR}} \tag{1}$$

With n_s the gas species number density of species s in the CSTR unit, t the time and $S_{rxn,\,s}$ the change in number density of species s due to reactions. The second and third terms on the right-hand side correspond to the flow entering and leaving the CSTR unit, respectively. Here, $n_{s,\,in}$ and $n_{s,\,out}$ are the number densities of species in the in- and outflow, respectively, while v_{in} and v_{out} are the volumetric flow rates that enter and leave the CSTR, respectively. Note that the species number density in the outflow equals that in the CSTR unit, i.e., $n_s = n_{s,\,out}$. V_{CSTR} is the volume of the CSTR unit.

The change in gas species number densities due to reactions is calculated as:

$$S_{rxn,s} = \sum_{i,\,gas} (c^R_{s,i} - c^L_{s,i}) r_i + n_{sites} \sum_{i,\,surf} (c^R_{s,i} - c^L_{s,i}) r_i \tag{2}$$

The first term on the right-hand side represents the summation of the net reaction source terms over the gas reactions, while the second term represents the sum of the net source terms for surface reactions. Inside the sum, $c^R_{s,\,i}$ and $c^L_{s,\,i}$ are the stoichiometry coefficients of species s in reaction i, at the right-hand (R) and left-hand (L) side of the reaction equation, respectively. Thus, $c^R_{s,\,i}$ and $c^L_{s,\,i}$ are the number of molecules s that are formed or lost,

respectively, in reaction i. Additionally, r_i is the rate of the reaction and n_{sites} is the number of surface sites relative to the gas volume. The value of n_{sites} is set to 10^{22} sites m^{-3}, which corresponds to the surface over volume ratio of the tubular reactor ($2/R = 10^2$ m^{-1}) multiplied by a typical surface site density of 10^{20} sites m^{-2}.[32,33]

Similar to Eqs. (1) and (2), the time-evolution of the fractional coverages (θ_s) of the surface species is described by:

$$\frac{\partial \theta_s}{\partial t} = \sum_{i,\, surf} (c_{s,i}^R - c_{s,i}^L) r_i \tag{3}$$

Since the adsorbates do not move along with the gas flow, the flow terms are omitted in Eq. (3).

For the first CSTR unit, $n_{s,\,in}$ and v_{in}, in Eq. (1) are the species densities and flow rate of the feed. For the subsequent CSTR units, $n_{s,\,in}$ and v_{in} match $n_{s,\,out}$ and v_{out} of the previous unit. For each CSTR unit, the volumetric flow rate leaving the reactor, v_{out} in Eq. (1), is calculated as the sum of volumetric flow rate entering the reactor and the change in volume due to reactions:

$$v_{out} = v_{in} + \frac{V_{CSTR} k_b T_{gas}}{p_{tot}} \sum_{s,gas} S_{rxn,s} \tag{4}$$

With k_b the Boltzmann constant, T_{gas} the gas temperature and p_{tot} the total pressure. The sum of the reaction source terms $S_{\mathrm{rxn},\,s}$ (see Eq. (2)) is taken over all gas species.

The reactions rates r_i in Eqs. (2) and (3) are calculated from the rate coefficients k_i, the number densities n_s or fractional coverages θ_s (for gas or surface species, respectively) of the reactants, and their stoichiometry coefficients $c^L_{s,\,i}$:

$$r_i = k_i \prod_{s,\,gas} (n_s)^{c^L_{s,i}} \prod_{s,\,surf} (\theta_s)^{c^L_{s,i}} \tag{5}$$

A list of the reactions with their corresponding rate coefficients is included in Table S1 of the supporting information (SI). Additionally, in Sect. "Solving the Boltzmann equation for electrons" to "Correction for diffusion to the wall" we provide more information on the calculation of the rate coefficients for electron impact and surface reactions. The gas phase reactions, including electron impact processes, are taken from the CO_2 part of the chemistry set presented by Slaets et al.[48, 49] for CO_2/CH_4 plasma, to which we added reactions for $CO(A^3P)$, $O(^1D)$, CO_3^- and CO_4^-. Likewise, the list of electron impact cross sections is also taken from Slaets et al.[48, 49]

Solving the Boltzmann Equation for Electrons

To calculate the electron energy distribution function (EEDF) and the rate coefficients of the electron impact reactions, our model requires a solver for the electron Boltzmann equation. For this purpose, we use BOLOS,[45] an open-source Python library containing a Boltzmann solver, that is based on the work of Hagelaar and Pitchford [46]. This algorithm calculates the EEDF, the rate coefficients for electron impact reactions and the electron

mobilities μ_e, for a specified gas mixture and reduced electric field *E/N* (i.e., ratio of electric field over gas number density, an important parameter to characterize the plasma conditions). Additionally, BOLOS requires the cross sections of the relevant electron impact processes. A list of these processes with the sources of the corresponding cross sections can be found in Table S2 in the SI.

The reduced electric field *E/N* is related to the power density *P* in the plasma via:

$$\frac{E}{N} = \frac{1}{N}\sqrt{\frac{P}{n_e e \mu_e}} \tag{6}$$

With *E* the electric field, *N* the total gas species number density, n_e the electron density, *e* the elementary charge and μ_e the electron mobility. Hence, the model determines the value of the *E/N* that corresponds to a specified power density, by combining Eq. (6) with BOLOS, which relates μ_e to the *E/N*.

During the numerical integration (i.e., as the code solves the system of differential equations provided by Eqs. (1) and (3)), the reaction rates of electron impact processes are calculated with BOLOS by solving the EEDF for the corresponding E/N. The E/N itself is calculated from Eq. (6) during the integration, while μ_e is kept constant. Hence, the E/N and corresponding electron impact reaction rates (from BOLOS) are continuously (re)calculated during the integration, while μ_e remains constant. This leads to a (small) drift of the power density *P* during the integration. After each integration period, the value of μ_e is therefore updated by iterating over Eq. (6) and BOLOS to acquire the values of E/N and μ_e that correspond to the actual set power density. The model then calculates the length of the next timestep over which is integrated, based on the deviation of the power density during the previous step, so that the deviation of the set power density remains below 1% during each integration period.

Rate Coefficients for Glass Surfaces

The reactor walls in our model are either catalytic transition metals or non-catalytic borosilicate glass surfaces. While the reactions on the former are described using TST combined with DFT data (see Sect. "Density functional theory calculations"), the reactions on the glass surface are treated with empirically determined expressions that are commonly used in literature, a more in dept discussion of which can be found in refs. [32–34]. We consider the following reaction types in our model:

- Physisorption.
- Chemisorption.
- Desorption (of chemisorbed and physisorbed species).
- Surface diffusion from a physisorption to a chemisorption site.
- Langmuir-Hinshelwood (L-H) reactions between a physisorbed and a chemisorbed species.
- Langmuir-Rideal (L-R) reactions between a gas species and a chemisorbed or physisorbed species.

Note that some recent works consider additional reactions, such as the formation of metastable chemisorption sites,[50] or O_3 formation on the surface [51]. However, we here limit ourselves to the most general and commonly used reactions for glass surfaces, because we aim to keep the chemistry on the glass surface relatively simple, as the focus of this work is on the catalysts.

As is apparent from the glass surface reactions listed above, two types of surface sites are considered, namely physisorption ($*^p$) and chemisorption ($*^c$) sites. Note that the distribution between chemisorption and physisorption sites varies widely in literature for different SiO_2-based surfaces (e.g., values between 2×10^{-3} and 0.25 are mentioned in ref.[32] for the fraction of chemisorption sites). In our model, we use a chemisorption site fraction equal to 2×10^{-3} in accordance with ref.[32], and the remaining site fraction (0.998) consists of physisorption sites. Similarly, a large range of values are reported in literature for the recombination coefficient γ, i.e., the fraction of radicals that recombines at the wall surface upon collision with the wall [27]. For example, Paul et al.[27] reviewed γ values for O atom recombination on various Materials and reported values between 10^{-5} and 10^{-2} for glass-based surfaces around room temperature (r.t.). Possible explanations for this large deviation include the possible role of impurities as chemisorption sites, or chemisorption sites being created as a result of ion-bombardment on the surface [27, 32].

In this regard, Booth et al.[52] found that for an O_2 DC glow discharge inside a pyrex tube the γ values decreased with lowering the pressure until 0.75 Torr (1.0 mbar), below which γ increased with further lowering the pressure. The authors found that below approximately 0.3 Torr, ions and fast neutrals incident on the wall have sufficient energy to clean or modify the surface, and hence attributed this effect to surface bombardment by energetic species [52]. This was further expanded upon by, Afonso et al.,[50] who developed a kinetic model that includes surface modification by energetic plasma species to form metastable chemisorption sites. The authors compared their modelling results to experiments to derive the values of certain surface parameters used in their model, and were also able to reproduce the experimental results [50]. However, we did not include such effect in our own model, as surface modification by the plasma is outside the scope of this study. Nevertheless, it is worth noting that surface bombardment and modification by energetic plasma species, leading to, e.g., different site types, may also occur on transition metal catalysts [53].

Note that glass is included in our model as a non-catalytic reference surface, to compare to the catalytic transition metals. Hence, only highly reactive radicals can adsorb (physisorption or chemisorption) on glass, while dissociative adsorption of stable molecules is not considered for this surface, because of its non-catalytic nature.

In the following subsections we describe the different surface reactions and their corresponding rate coefficients. A list of the surface reactions that are included in our model for the glass surface can be found in the SI, Table S3.

Physisorption and Chemisorption The rate coefficients for adsorption of radicals on both physisorption and chemisorption sites are described using the Hertz-Knudsen equation (i.e.,

the flux to the surface, because radicals have 100% adsorption probability, and they are the only species considered for adsorption on the glass surface):

$$k = k_b T_{gas} \frac{A_s}{\sqrt{2\pi\, m k_b T_{gas}}}$$

With m the mass of the impinging gas species and A_s the surface sites area, which is set to 10^{-20} m^2, i.e., the inverse of the surface site density. The factor $k_b T_{gas}$ is included to convert the gas species number density, which is multiplied with the reaction coefficient in the calculation of the rate in Eq. (5), to the corresponding partial pressure.

Desorption The rate coefficient for desorption from both physisorption and chemisorption sites is given by:[32, 34, 52]

$$k = \nu_d \exp\left(-\frac{E_d}{R_{gas} T_{wall}}\right) \tag{8}$$

In this formula, v_d is the vibrational frequency for the movement of the adsorbate perpendicular to the surface, for which we use a typical value of 10^{15} s^{-1}.[32] R_{gas} is the ideal gas constant, T_{wall} is the wall temperature, which we consider equal to the gas temperature T_{gas} (as explained above) and E_d is the activation energy for desorption. We use a value of 0.302 eV as the activation energy for desorption of physisorbed O, based on ref. [52], and 2.90 eV for desorption of chemisorbed O, based on ref.[33]. Note that in ref.[52], a lower value of 10^{13} s^{-1} was used for v_d, as this led to better agreement with their experimental values for the recombination coefficient γ. However, in that study the recombination of O atoms through L-H reactions was not considered in the surface chemistry. We found that using the typical value of 10^{15} s^{-1} for v_d and including L-H reactions in the chemistry set, results in γ values that are comparable to those measured in ref.[52], which was also mentioned by Viegas et al.[51] Hence, this justifies combining the empirically determined value for E_d from ref.[52], with the more generally used value of 10^{15} s^{-1} for v_d. However, it must be noted that Ibach et al.[54] pointed out that v_d should be temperature dependent. More recently, Viegas et al.[51] developed a model for surface recombination on a Pyrex surface in contact with an O_2 DC glow discharge and compared their results to experimental measurements. The authors observed an exponential decrease of v_d with the wall temperature (for T_{wall} between 253 and 323 K), which they mentioned could also be explained by a variation of the activation barrier for desorption with coverage, i.e., since the coverage rises as the temperature drops [51]. Moreover, Ibach et al.[54] find a quadratic rather than an exponential dependency of v_d on temperature for adsorbates that have lost all three translational degrees of freedom (as is the case for activated surface diffusion), yet also predict that v_d is proportional to $\exp(\theta_{ads}/(1- \theta_{ads}))$ when lateral interactions between adsorbates are present [54]. Hence, it is more likely that the exponential decrease of v_d at lower wall temperature observed experimentally by Viegas et al.[51] is the result from higher coverages and lateral interactions between the adsorbates. Nevertheless, we choose to treat v_d

as a constant in our model for simplicity, and due to the uncertainties associated with the temperature dependency.

Surface Diffusion The surface diffusion coefficient of a physisorbed species to a chemisorption site is calculated according to:[32, 33]

$$k = \frac{\nu_D}{4} \exp\left(-\frac{E_D}{R_{gas} T_{wall}}\right) \tag{9}$$

With v_D the frequency for vibration of the adsorbate in the direction parallel to the surface and E_D the activation barrier for diffusion to an adjacent site. We use a typical value of 10^{13} s^{-1} for v_D,[32, 33, 55] while E_D is approximated by $E_d/2$.[32, 55]

Langmuir-Rideal Reactions The formula for the rate coefficients of L-R reactions takes a similar form as Eq. (7), but contains an exponential factor with the activation energy of the reactions, i.e., representing the probability of the reaction occurring upon collision with an adsorbate:[32–34]

$$k = k_b T_{gas} \frac{A_s}{\sqrt{2\pi\, m k_b T_{gas}}} \exp\left(\frac{-E_r}{R_{gas} T_{gas}}\right) \tag{10}$$

The parameter E_r in the exponential factor is the activation energy for recombination between the adsorbate and the incoming gas species. As an approximation we use the same activation energy for L-R reactions involving chemisorbed or physisorbed species as the adsorbate. For recombination of two O atoms via L-R, we use E_r = 0.13 eV, which was experimentally determined for O_2 plasma in a Pyrex tube [52]. We also include an L-R reaction between gaseous CO and an adsorbed O atom, for which we use an activation energy of 0.10 eV, as experimentally determined in ref.[56] for a borosilicate glass-based heatshield coating.

Langmuir-Hinshelwood Reactions The rate coefficient for recombination between a physisorbed and a chemisorbed O atom takes a similar form as Eq. (9), but with an additional exponential factor containing the activation energy for recombination:[32]

$$k = \frac{\nu_D}{4} \exp\left(-\frac{E_D}{R_{gas} T_{wall}}\right) \exp\left(-\frac{E_r}{R_{gas} T_{wall}}\right) = \frac{\nu_D}{4} \exp\left(-\frac{E_D + E_r}{R_{gas} T_{wall}}\right) \tag{11}$$

As such, the extra exponential factor takes into account the probability for recombination to occur upon diffusion of a physisorbed O atom to an occupied O chemisorption site. The values of E_r for L-H in Eq. (11) and L-R in Eq. (10) are considered to be the same [32].

Note that some models [34, 50, 51] also consider L-H recombination between physisorbed atoms, which is assumed to occur with E_r = 0.0 eV, i.e. so that the reaction barrier becomes E_D. The assumption that the recombination between physisorbed atom is barrier-

less (except for the barrier associated with diffusion) is based on the fact that physisorbed atoms only weakly interact with the surface. This reaction was studied computationally by Marinov et al.[34] who investigated the effect of varying its activation barrier, and compared the contribution of the reaction to the total recombination coefficient γ. Even at E_R = *0.0 eV* the contribution of L-H between two physisorbed O atoms only became important below a wall temperature of 300 K, as the coverage of physisorbed atoms rises at lower temperatures [34]. Since our simulations are performed at relatively high temperatures of 500–1100 K, we do not consider this reaction here as it is not expected to be important, and because of the uncertainties associated with its recombination barrier.

Lastly, we would like to mention that there is a lot of variation in the values of the different parameters governing the glass surface kinetics reported in literature [32]. We have therefore investigated how varying these parameters affects our results for a single set of conditions, and we discuss these results in the SI, section S4.

Rate Coefficients for Transition Metals

We consider four reaction types on the transition metal surfaces: adsorption, desorption, L-H reactions and L-R reactions. As we calculate DFT energies for pure metal (111) surface facets, without lattice defects or impurities, we consider only one site type on which species can adsorb. This is in contrast with the glass surface used in our model, for which both weak (i.e., physisorption) and strong (i.e., chemisorption) binding sites are considered, in accordance with the empirical models described in literature [32, 33]. As only one site type is considered for transition metals, surface diffusion (i.e., between different site types) is not included in the model for the metal surfaces.

For adsorption, desorption and L-H reactions, the corresponding rate coefficients are based on the energies calculated with our DFT simulations. For the L-R reactions, however, the DFT energies were combined with recombination coefficients from literature to estimate the values of the associated rate coefficients. In the following sections we describe how these rate coefficients, and their corresponding activation and reaction energies, are calculated.

Adsorption and Desorption The rate coefficients for molecular adsorption are not described by TST, but instead by the Hertz-Knudsen equation multiplied by an enthalpy-based sticking coefficient:

$$k_{ads} = k_b T_{gas} \frac{A_s}{\sqrt{2\pi\, m k_b T_{gas}}} \exp\left(\frac{-\Delta\, H^{\ddagger}_{ads}}{R_{gas} T_{gas}}\right) \tag{12}$$

If adsorption is endothermic, $\Delta H^{\ddagger\circ}_{ads}$ is set equal to the standard reaction enthalpy. However, in most cases adsorption is exothermic and $\Delta H^{\ddagger\circ}_{ads}$ is set to zero, so that the sticking coefficient becomes one and Eq. (12) becomes equal to the Hertz-Knudsen equation. The rate coefficient for the corresponding reverse reaction, i.e., desorption, is calculated through detailed balancing:

$$k_{des} = \frac{k_{ads}}{K_{eq}} \frac{p^o}{k_b T_{gas}} \tag{13}$$

In Eq. (13), the factor $p°(k_bT_{gas})^{-1}$ corresponds to the number density at the standard pressure $p°$, which is 10^5 Pa (1 bar). This is required to have consistent units, and because the equilibrium constant K_{eq} is determined from DFT data, which were calculated for a reference pressure of 1 bar. The equilibrium constant is described by:

$$K_{eq} = \exp\left(-\frac{\Delta\, G^o_{rxn}}{R_{gas}T_{wall}}\right) = \exp\left(-\frac{\Delta\, H^o_{rxn}}{R_{gas}T_{wall}}\right)\exp\left(\frac{\Delta\, S^o_{rxn}}{R_{gas}}\right) \tag{14}$$

In which $\Delta G°_{rxn}$, $\Delta H°_{rxn}$ and $\Delta S°_{rxn}$ are the standard reaction Gibbs free energy, enthalpy and entropy, respectively, of adsorption, obtained from our DFT calculations (see below, and Table S4 in the SI).

Langmuir-Hinshelwood Reactions The rate coefficients for reactions happening on transition metal surfaces are calculated using TST:

$$k = \frac{k_b T_{wall}}{h}\exp\left(-\frac{\Delta\, G^{\ddagger}}{R_{gas}T_{wall}}\right) = \frac{k_b T_{wall}}{h}\exp\left(-\frac{\Delta\, H^{\ddagger}}{R_{gas}T_{wall}}\right)\exp\left(\frac{\Delta\, S^{\ddagger}}{R_{gas}}\right) \tag{15}$$

With h the Planck constant, and $\Delta G^{\ddagger}°$, $\Delta H^{\ddagger}°$ and $\Delta S^{\ddagger}°$ the standard Gibbs free energy, enthalpy and entropy, respectively, between the transition and initial state, again obtained from our DFT calculations (see below, and Table S4 in the SI). Note again that in our model T_{wall} is set equal to T_{gas}. The entropy of the surface species (adsorbates and transition states) is calculated using the harmonic oscillator approximation. Hence, all degrees of freedom in the surface species are treated as vibrational modes.

Reaction and Activation Energies The Gibbs free reaction energy is defined as the difference between the standard Gibbs free energies of the products and the reactants:

$$\Delta\, G^o_{rxn} = \sum {}_{products} G^o_s - \sum {}_{reactants} G^o_s \tag{16}$$

Similarly, the Gibbs free activation energy is calculated as the difference between the Gibbs free energies of the transition state (TS) and the reactants. However, we ensure that the activation energy is never negative or below the reaction energy:

$$\Delta\, G^{\ddagger} = \max\left(\left(\sum {}_{TS} G^o_s - \sum {}_{reactants} G^o_s\right),\ \Delta\, G^o_{rxn},\ 0\right) \tag{17}$$

The standard Gibbs free energies $G°_s$ of the individual species are calculated from the (corrected) species enthalpies $H°_s$ and entropies $S°_s$, which are acquired from DFT:

$$G^o_s = H^o_s - E_{ZPE} + H_{s,\,0K\to T} - TS^o_s \tag{18}$$

In which E_{ZPE} is the zero-point energy correction, $H_{s,0\,K\rightarrow T}$ is the correction for the change in enthalpy with temperature, T is the wall or gas temperature (both are the same in our model) and S_s is the temperature-dependent species entropy. For surface species, the entropy and correction on the enthalpy are acquired via the harmonic oscillator approximation, as described in ref.[57]. This requires the vibrational frequencies of the surface species, which are acquired from our DFT calculations and are listed in Table S4 in the SI, together with the species enthalpies. For gas species, the enthalpy correction and entropy are calculated using the ideal gas approach, which is also described in ref.[57]. The values of the parameters used in the ideal gas approximation are listed in Table S5 in the SI along with their corresponding sources.

Simplified Expression for the Rate Equations To simplify the expressions of the reaction rate coefficients used for transition metal surfaces in the model, while also including the correction on the enthalpy and entropy, we calculate the values of the rate coefficients for the temperature range 100–1200 K and fit these to a modified Arrhenius expression:

$$k = a \times T^{b} \exp\left(\frac{c}{T}\right) \tag{19}$$

In which a, b and c are fitting parameters. Equation (19) is frequently used in literature to describe rate coefficients that have a more complex dependence on temperature than described by the simple Arrhenius equation (i.e., for which b = 0).[58, 59] Note that we only use this approach for the rate coefficients of adsorption, desorption, and L-H reactions on the transition metal surfaces. The rate coefficients acquired by fitting to Eq. (19) can be found in the SI, Table S6. By fitting our calculated rate coefficients to Eq. (19), we acquire a simple expression that incorporates the effect of the temperature-dependent entropy and correction on the enthalpy, without the requirement to recalculate these thermodynamic quantities at each temperature. This facilitates the use of the rate coefficients calculated in this work by other researchers, especially for simulations in which the temperature is not constant.

Langmuir-Rideal Reactions There is still much uncertainty on the kinetics of various L-R reactions and their importance in plasma catalysis [60]. In kinetic models for plasma catalysis, the rate coefficients for L-R reactions are often calculated using collision theory combined with (estimated) sticking coefficients,[19, 61–65] or by TST in which the enthalpy barrier is varied or assumed zero [12, 15]. Using a microkinetic model for NH_3 synthesis, Engelmann et al.[12] illustrated that if L-R reactions would occur without enthalpy barrier, this should result in high reaction rates for all transition metal catalysts used, yielding a flat volcano curve when viewed on a logarithmic scale, in agreement with experimental data [66]. On the other hand, various experimental studies show that for O atom recombination on transition metal surfaces, most metals have indeed a high catalytic activity, although there exist clear (yet less extreme) differences between the different metals [27, 67–70]. Additionally, as we will explain in the Results and Discussion section, our simulations show that the high recombination coefficients for O atoms on transition metals cannot be explained based on L-H reactions alone. Instead, we propose that at relatively low

temperatures (≤600 K), recombination of O atoms on metal surfaces occurs through an L-R reaction between an impinging and a pre-adsorbed O atom. Only at higher temperatures, O_2 formation via L-H between adsorbed O atoms becomes relevant. Assuming that the rate coefficients for adsorption and L-R can be described by Eqs. (7) and (10), respectively, the activation energy for L-R can be calculated from the recombination coefficient γ (i.e., by solving the species balance equations at steady state):

$$E_r = -R_{gas} T ln\left(\frac{\gamma}{2-\gamma}\right) \tag{20}$$

May et al.[70] reported values of 0.22 and 0.063 for the recombination coefficient of O at r.t. on Ag and Cu surfaces, respectively. Using Eq. (20), the corresponding values for the activation energy are calculated as 5.2 and 8.5 kJ/mol (0.054 and 0.088 eV) for Ag and Cu, respectively.

To the best of our knowledge, there are no experimentally measured γ values for O recombination on Pd or Rh surfaces available in literature. Nevertheless, experimental studies [67–70] show that the activity of a metal for O atom recombination can be linked to its chemical character (i.e., noble metal or not). Hence, γ is typically the highest on Ag ($\sim 10^{-1}$ at r.t.), followed by Cu ($\sim 10^{-1}$–10^{-2} at r.t.) and non-noble metals, like Fe ($\sim 10^{-2}$ at r.t.) and Ni ($\sim 10^{-2}$ at r.t.). Note that exceptions to this rule do exist, most notably for Au, which has a relatively low γ ($\sim 10^{-2}$–10^{-3} at r.t.) [67, 69, 70]. The observed trend appears to be the result of the formation of either bulk metal oxide or a thin oxidation layer on the surface of most metals [67–70]. Consequently, more stable metal oxides result in a lower catalytic activity (i.e., a lower γ value) of the corresponding metal. Indeed, if O binds less strongly to the metal, it will be easier to remove the O atom from the metal surface (or oxide layer) during the L-R reaction with an impinging radical from the gas phase [69].

Hence, we assume a linear correlation between the O binding strength of the metal and its barrier for O recombination via L-R. Using the activation energies that we calculated for Ag and Cu, and the O atom adsorption energies calculated from DFT, we then estimate the values of the activation energies on Pd and Rh to be 7.6 and 9.6 kJ/mol (0.079 and 0.10 eV), respectively. At 300 K this corresponds to γ values of 0.09 and 0.04, respectively, which is in the same range as typical values for other transition metals reported in literature [27]. Note that we do not consider the formation of a bulk oxide in our simulations, however the formation of a layer of adsorbed O atoms can be seen as an initial step in oxidation of the metal.

In some of our simulations we also study the potential influences of the L-R reactions between an adsorbed CO* molecule and an incoming O atom (see Sect. "Effect of L-R reactions in plasma-catalytic CO2 splitting"). Since this requires the O atom to attack the C atom from CO* (which is directed towards the surface), the reaction must be highly entropically constrained. Therefore, we describe the rate coefficient for this reaction using Eq. (15) and assume an entropy barrier equal to the loss of (translational) entropy of the impinging O atom. The enthalpic part of the activation barrier is assigned a value between 0 and 0.2 eV to illustrate its effect on the reaction.

Correction for Diffusion To the Wall

To consider that the loss of species at the reactor wall may be limited by their rate of diffusion to the wall, we apply a correction factor to the rates of adsorption and L-R reactions. The mean lifetime (inverse loss frequency) of a species due to wall recombination can be expressed as the sum of the mean time required for diffusion to the wall and that for reaction at the wall:[71, 72]

$$\tau = \tau_{diff} + \tau_{net\ loss} \tag{21}$$

The mean time for diffusion to the wall τ_{diff} is calculated from the characteristic diffusion length of the reactor Λ_0 and the diffusion coefficient D:[71, 72]

$$\tau_{diff} = \frac{\Lambda_0^2}{D} = \left(\frac{R}{2.405}\right)^2 \frac{1}{D} \tag{22}$$

In which $\Lambda_0 = R/2.405$, with R the radius of the reactor. The diffusion coefficient of the gas species is estimated using:[72]

$$D = \frac{1}{3} l v_{th} = \frac{1}{3} \left(\frac{k_b T_{gas}}{\sqrt{2} \cdot\ p\pi\ d^2}\right) \sqrt{\frac{8 k_b T_{gas}}{\pi\ m}} \tag{23}$$

With l the mean free path, v_{th} the thermal velocity of the gas species, p the pressure, m the mass of the species and d the kinetic diameter of the molecule. The values of d for CO_2, CO and O_2 are equal to 330 ppm, 376 ppm and 346 ppm, respectively [73]. The value for O atoms is assumed similar to that of O_2.[72]

The mean lifetime $\tau_{net\ loss}$ of gas species near the surface before consumption due to surface reactions (i.e., adsorption, L-R) is typically described by the recombination coefficient γ and the thermal velocity of the gas species. However, in our model, the recombination of gas species at the surface is not considered as a single reaction step. Instead, we use a detailed reaction mechanism in which the different surface reactions (adsorption, desorption, L-H, L-R, etc.) are included as separate reactions steps. Moreover, as long as steady state is not reached, atoms and molecules can accumulate on the surface. Hence, we calculate the mean lifetime of a gas species before it is consumed by surface reactions (when the reaction is not diffusion-limited) as:

$$\tau_{net\ loss} = \frac{n_s}{n_{sites} \sum_{i,\ surf} (c_{s,i}^L - c_{s,i}^R) r_i} \tag{24}$$

In which the numerator equals the species density, and the denominator is the source term for the net loss of the gas species s due to surface reactions (e.g., adsorption, L-R). We use the same notation for the overall lifetime (= inverse loss frequency), but here we also include a correction factor f_s to take the effect of diffusion into account. If the loss of a gas species at the wall is limited by diffusion, the density of this species near the wall will decrease, limiting the consumption rate at the wall surface. By combining Eqs. (21) and (24) we get:

$$\frac{n_s}{n_{sites}\sum_{i,\,surf}(f_s c^L_{s,i} - c^R_{s,i})r_i} = \tau_{diff} + \frac{n_s}{n_{sites}\sum_{i,\,surf}(c^L_{s,i} - c^R_{s,i})r_i} \quad (25)$$

Which can be rearranged into:

$$f_s = \left(\left(\frac{\tau_{diff}}{n_s} n_{sites} + \frac{1}{\sum_{i,\,surf}\left(c^L_{s,i} - c^R_{s,i}\right) r_i}\right)^{-1} + \sum_{i,\,surf} c^R_{s,i} r_i\right) \cdot \left(\sum_{i,\,surf} c^L_{s,i} r_i\right)^{-1} \quad (26)$$

The rate equations for adsorption and L-R reactions are then multiplied by the correction factor f_s of the gaseous reactant. In this way the overall loss of a gas species due to surface reactions cannot exceed the rate for diffusion of the species to the wall. Note that f_s is set to 1 if $\sum_{i,\,surf}(c^L_{s,i} - c^R_{s,i})r_i$ is negative, i.e., if the gas species is net produced at the wall surface. Hence, f_s can have values between 0 and 1. As such, f_s becomes 1 if the effect of diffusion is negligible and the loss of species at the surface is not diffusion-limited. If recombination of species at the surface is fast, the rate becomes limited by diffusion to the surface and the value of f_s drops.

We find that for the conditions under study, $f_s \approx 1.0$ for loss of O atoms on the glass surface. Hence, due to the low γ values for glass, the loss of O atoms to the surface is not limited by diffusion and the O atom density can be considered uniform along the radial direction. This agrees with the work by Viegas et al.[74] for low-pressure DC O_2 glow discharges at 1–10 Torr (1.3–13.3 mbar), who found that the O(^{3}P) density along the radial direction has an almost flat profile, based on 1D fluid dynamics simulations. Nevertheless, we find that the effect of diffusion to the wall is relevant for the transition metals at most of the conditions under study. Indeed, transition metals typically have higher γ values for O atom recombination than glass [27]. Hence, the fast loss of O atoms to the transition metal surfaces causes the rate to become limited by diffusion to the walls. For the conditions under study, we find that the f_s values vary between 9.9×10^{-2} and 5.1×10^{-3} for Ag, 1.9×10^{-1} and 1.3×10^{-2} for Cu, 1.0 and 7.6×10^{-3} for Pd, and 1.0 and 1.5×10^{-2} for Rh.

Results and Discussion

The purpose of this study is to investigate how different transition metal catalysts affect the recombination of radicals in plasma catalysis, which can both positively or negatively impact the conversion, depending on the catalyst and conditions, like temperature, pressure, and flow rate. Our combined plasma-surface microkinetic model simulates the reaction kinetics, both in the gas phase and at the catalyst surface, for a low-pressure CO_2 discharge in a cylindrical reactor with either a glass wall or a transition metal wall that functions as the catalyst. The reactor is modelled as an initial discharge region (with glass wall) with a length of 5.0 cm, followed by a 50.0 cm long afterglow region, with a glass or transition metal wall surface.

Regarding the plasma-catalyst interactions, we focus exclusively on the exchange of radicals and ground-state molecules between the plasma and the surface. We do not consider the effect of vibrationally excited species on the surface chemistry, because of the following reasons. Multiple microkinetic models have already studied the effect of vibrational excitation on various plasma-catalytic reactions, including NH_3 synthesis,[9, 10, 12] CH_4

non-oxidative coupling,[11, 19] CH_4 partial oxidation,[15] CO_2 hydrogenation [14] and N_2 oxidation [16, 17]. In these studies, the Fridman-Macheret (FM) α model [75] is used to describe the drop in activation barrier for surface reactions involving vibrationally excited species. However, the FM model is originally intended for gas phase reactions,[75] and is a rough approximation. Moreover, the aforementioned microkinetic models [11, 12, 14–17] predict that the vibrationally excited species have only a minor effect compared to plasma-produced radicals, while both result in more facile reactant activation. It should however be noted that a recent study [76] shows that the FM model significantly underestimates the effect of vibrational activation on dissociative adsorption, when compared to values calculated using molecular dynamics simulations, which also illustrates the inaccuracy of the FM model. Additionally, based on the Polanyi-rules,[77] dissociative adsorption of CO_2 is expected to have high efficiencies for vibrational activation, due to its late transition state [78]. Yet, as we aim to disentangle the contributions of radicals and vibrationally excited species on the surface chemistry, and want to avoid the use of the inaccurate FM model, we focus exclusively on the effect of radicals and ground-state molecules. The effect of vibrational excitation on the surface kinetics will, however, be investigated in future work by our research group.

Note that the model and the different components of the chemistry set could unfortunately not yet be validated with experiments, since, to the best of our knowledge, only very limited diagnostic experimental data is available for low pressure CO_2 RF discharges, on which we based our model. Moreover, the focus of this work is primarily on the interaction of the plasma species (CO, O_2 and O) with the transition metal catalysts, for which model validation against plasma diagnostic data would not be sufficient. Indeed, validation should be carried out by in-situ catalyst surface diagnostics, for which unfortunately also no experimental data could be found in literature. Hence, the reader should be aware that our model has no predictive character, but it can hopefully still provide qualitative trends, and useful insights in the underlying mechanisms, and in suitable catalysts and operating conditions. For validation of the model and chemistry set in possible future work, we suggest simulating a low-pressure CO_2 DC glow discharge, for which more detailed experimental diagnostics are available, such as the work by Morillo-Candas et al.[72] However, we believe it would be beneficial to first optimize and validate the chemistry for recombination of O atoms on the glass surface, by comparing simulation results of low-pressure O_2 DC glow discharges, against diagnostic experimental data, which is readily available in literature [52, 79].

In the following subsections, we will first illustrate the importance of L-R reactions for O atom recombination into O_2, as well as the potential effect of L-R reactions for CO oxidation back into CO_2. Next, we will discuss the reaction mechanisms and kinetics of CO_2 splitting in a low-pressure plasma and its afterglow exposed to a non-catalytic (glass) or catalytic (Ag) surface, for a single set of representative conditions. This serves as a basis for the following sections in which we will discuss how different types of transition metals can both positively and negatively affect plasma-catalytic CO_2 splitting. Moreover, we will show that whether a catalyst has a positive effect on the conversion, does not only depend on the type of transition metal, but also on conditions, like temperature, pressure and flow rate. Hence, the same type of catalyst can differently affect CO_2 conversion, depending on the reaction conditions. We will end with a discussion on the optimal catalyst properties, i.e., which transition metal catalyst would be beneficial for (post-)plasma catalysis, and at which reaction

conditions. We base this discussion on material characteristics of the catalysts (weakly or strongly binding) and the insights obtained by our model.

Importance of Langmuir-Rideal Reactions for O Atom Recombination

To illustrate the importance of L-R reactions for O atom recombination, we compare the evolution of the calculated O atom fractions for chemistry sets with and without L-R reactions, for a pure O_2 plasma. Note that our model does not distinguish between "true" L-R reactions and "hot atom" reactions. In the former, a gas species collides and reacts directly with an adsorbate, while in the latter, a gas species hits the surface but does not fully adsorb and retains some of its energy, allowing it to move over the surface and react with a fully adsorbed species. Hence, in the framework of our model, L-R reactions refer to all reactions in which a gas species does not occupy a surface site prior to reaction with an adsorbate.

Figure 2 (a) illustrates the importance of L-R reactions for O recombination, by comparing the evolution of the mole fraction of O atoms in the afterglow of an O_2 plasma for different surface chemistry sets. We consider three cases, namely an Ag surface with and without the inclusion of L-R reactions, as well as a glass surface. Note that we do not show the results for other transition metals, as their curves largely overlap with those of Ag. Right after the plasma, i.e., the start of the afterglow, the O atom mole fraction is slightly below 0.5, with the remaining component being mainly O_2 molecules (slightly above 0.5), hence representing a dissociation degree of 32%. As can be seen in Fig. 2, the Ag chemistry set with L-R reactions results in the fastest drop in the fraction of O atoms, while Ag without L-R reactions shows the slowest consumption of O atoms, even compared to a glass surface. However, from literature it is clear that most transition metals, especially Ag, are highly active for O atom recombination, while glass surfaces are typically relatively inert for O atom recombination [27]. Indeed, most literature studies report γ values above 0.1 for Ag, while γ values for glass surfaces are typically between 10^{-2}–10^{-5}.[27] As such, the fraction

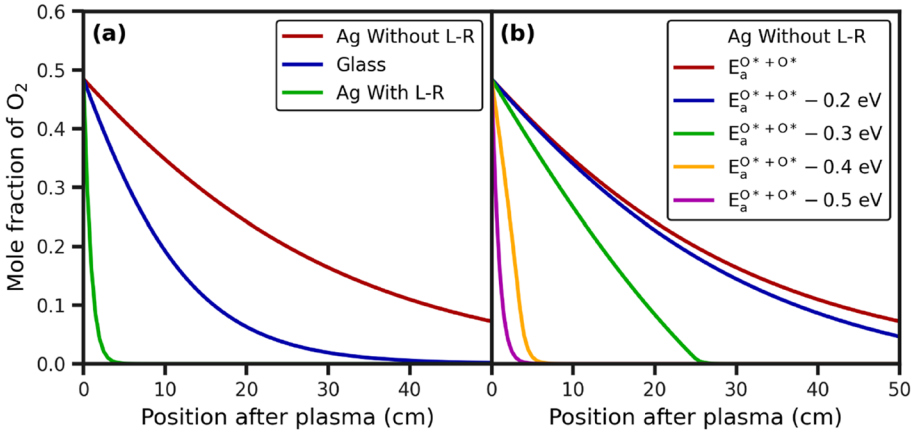

Fig. 2 Effect of the surface chemistry on the spatial evolution of the mole fraction of O atoms in the afterglow of an O_2 plasma. In (**a**) three surface chemistry sets are considered: an Ag surface, both with and without L-R reactions, as well as a glass surface. In (**b**) the effect of lowering the activation barrier of $O^* + O^* \rightarrow O_2^* + *$ is illustrated, for the Ag surface without L-R reactions. Conditions: T = 500 K, p = 5 mbar and flow rate = 100 sccm

of O atoms in the afterglow should decline much faster for an Ag wall compared to a glass wall. Hence, L-R reactions should play an important role in O atom recombination on transition metal surfaces. Indeed, we find that when only L-H reactions are considered for O atom recombination on the Ag surface, this reaction occurs very slowly (Fig. 2 (a)), which is not in agreement with the high recombination coefficients that are observed experimentally for this metal. We therefore suggest that a second type of surface reactions, namely L-R reactions, plays an important role in the recombination of O atoms on transition metal surfaces at 500 K.

While not shown in Fig. 2 (a), the O* coverages on the Ag surface are very high: above 0.99 when only L-H reactions are accounted for, and between 0.77 and 0.89 when L-R reactions are also considered. Hence the rate of the L-H reaction, which has a second order dependency on the O* coverage, is not limited by the availability of adsorbed O*, but instead by the low rate coefficient of this reaction at 500 K. Note that the O* coverages are slightly lower if O atom recombination via L-R is included in the chemistry set, as this reaction removes part of the adsorbed O*.

If we calculate the γ values for the conditions used in Fig. 2 (a), we find values of 0.44, 0.13, 0.16 and 0.10 for Ag, Cu, Pd and Rh, respectively, when L-R reactions are accounted for. When L-R are not included, however, the γ values are unrealistically low, with values in the order of Magnitude of 10^{-7}–10^{-8} for Ag, 10^{-16} for Cu, 10^{-15}–10^{-16} for Pd, and 10^{-19} for Rh. For reference, the recombination coefficient γ of the glass surface in Fig. 2 is equal to 2.0×10^{-4}.

The effect of L-R reactions is two-fold: on one hand it enables more facile production of O_2 compared to when only L-H reactions are considered, on the other hand it aids in the removal of adsorbed O* atoms from the surface. The latter results in lower O* coverages and thus less O* poisoning, which in turn improves adsorption of new O atoms from the gas phase, due to the higher availability of free surface sites. Note that as temperature rises, the contribution of L-H reactions may increase, as traversing the activation barrier becomes easier. While not shown in Fig. 2 (a), we find that as the temperature rises above 600–650 K, O atom recombination on transition metals via L-H reactions alone becomes sufficiently fast to reach the high recombination coefficients reported in literature for O_2 plasma.

Nevertheless, we must note that the high experimental recombination coefficients for O atoms on transition metals may also be caused by other effects than those of L-R reactions. For example, our model does not consider the destabilization of adsorbed O* atoms due to lateral adsorbate-adsorbate interactions, which may lower the barrier for O* atom recombination to O_2.[80–82] We therefore investigated how lowering the barrier for O* atom recombination via L-H affects our results for the Ag surface without L-R reactions. These results are displayed in Fig. 2 (b), which shows that lowering the activation barrier by 0.2 eV has only a small effect on the O_2 mole fraction in the afterglow, while reducing the activation barrier by 0.3 eV gives O_2 mole fractions that are similar to the glass surface in Fig. 2 (a). When the barrier is further decreased by 0.4 and 0.5 eV (Fig. 2 (b)), the O_2 mole fraction becomes comparable to the case where L-R reactions are considered Fig. 2 (a). Hence, if lateral adsorbate-adsorbate interactions between O* are sufficiently strong, so that the activation barrier for L-H reactions is lowered by approximately 0.4 eV, this effect may also explain the facile O* atom recombination on transition metal surfaces.

Lastly, a second effect that is not considered by our model is the formation of bulk oxides. Indeed, high surface coverages of O* atoms, i.e., similar to a thin oxide film, can initiate

the formation of bulk metal oxides [83]. Moreover, oxide formation is often reported in literature for metal surfaces exposed to a flux of O atoms [67–70]. Hence, the kinetics for adsorption and recombination of O atoms on bulk metal oxides, which do not necessarily occur via the same reaction mechanisms as on the corresponding transition metals, are likely to be important as well. This is, however, outside the scope of this work.

Effect of L-R Reactions in plasma-catalytic CO_2 Splitting

As discussed in Sect. "Importance of Langmuir-Rideal reactions for O atom recombination", we hypothesize that L-R reactions play an important role in the recombination of O atoms on transition metal surfaces. As O atoms are present in large amounts in CO_2 plasmas, surface recombination of O atoms into O_2 can also play an important role in plasma-catalytic CO_2 splitting. Importantly, if a catalyst surface can selectively recombine O atoms into O_2, thus avoiding that they recombine with CO back into CO_2, this could improve the overall CO_2 conversion.

To illustrate how L-R reactions can affect the recombination of O atoms in CO_2 splitting, we simulated a CO_2 plasma afterglow in contact with a Rh surface, again using different surface chemistry sets. These results are presented in Fig. 3, which shows the mole fractions of O atoms (a), O_2 (b), and CO (c) as function of position in the afterglow. Right after the plasma, i.e., the start of the afterglow, the O, O_2 and CO mole fractions are about 0.022, 0.0035 and 0.028, respectively, while the majority of the mixture is CO_2 with a mole fraction of 0.95. This corresponds to a dissociation degree of 2.9% for CO_2, and particle densities of 1.6×10^{15}, 2.3×10^{14}, 2.0×10^{15} and 6.9×10^{16} cm^{-3} for O, O_2, CO and CO_2, respectively. These mole fractions are calculated with our model for T = 500 K, p = 5 mbar, a Mass flow rate of 100 sccm, and a plasma power of 100 W (corresponding to an SEI of 13.8 eV/molecule). For comparison, Rond et al.[84] investigated CO_2 splitting in a RF plasma torch for pressures ranging from 1 to 2 mbar, Mass flow rates between 100 and 300 sccm, plasma powers between 80 and 160 W, and SEI's between 6.1 and 18.2 eV/molecule. These authors report CO_2 dissociation degrees between 2% and 13%, and CO and O densities ranging from 2×10^{14} to 8×10^{14} cm^{-3}.[84] Note that the dissociation degree is naturally larger at lower pressures. Hence, our calculated mole fractions are indeed representative for a low-pressure CO_2 RF plasma.

The red curves in Fig. 3 represent the results for a chemistry set in which only adsorption, desorption and L-H reactions are possible on the surface. For the blue curves, an additional (L-R) reaction is included, namely $O + O^* \rightarrow O_2 + *$, to which we refer as L-R1. As can be seen in Fig. 3 (a), the possibility for O atoms to recombine into O_2 via L-R1 results in a slight drop of the O mole fraction, yet the recombination of O atoms on the Rh surface remains quite slow. Indeed, the O mole fraction near the outlet is still about 83% of the value in the plasma for the blue curve. The slight drop in the O mole fraction is accompanied by a small rise in the mole fraction of O_2; see Fig. 3 (b), red and blue curves.

The reason that O recombination is slow on Rh for a CO_2 plasma, even if L-R1 is accounted for, is because of the strong CO-binding on this transition metal. As L-R1 results in the facile removal of O* from the surface, it lowers the O* coverage and thus enhances the fraction of free sites. Yet, on Rh these free sites are rapidly occupied by CO* molecules, as these bind strongly to the surface. This consequently leads to CO* poisoning of the surface, which keeps the catalyst activity low. Note that this is mainly a problem for strong

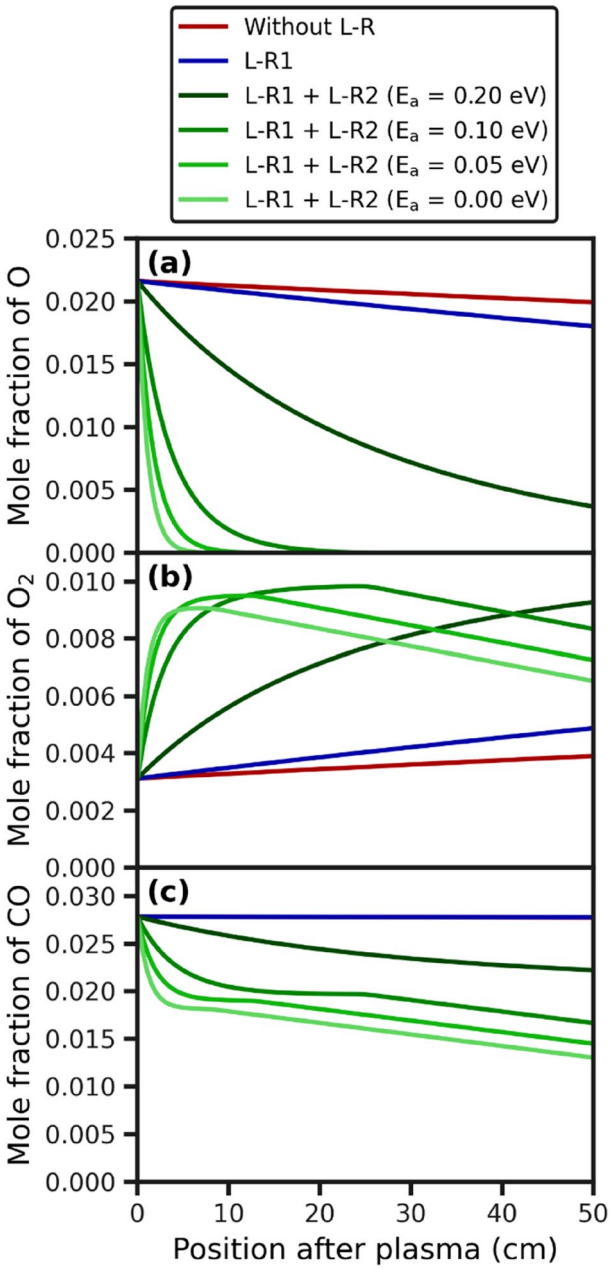

Fig. 3 Effect of L-R reactions on the spatial evolution of the mole fractions of O atoms (**a**), O_2 molecules (**b**), and CO molecules (c) for a CO_2 plasma afterglow in contact with a Rh surface. Two L-R reactions are considered: $O+O^* \rightarrow O_2 + *$ (L-R1) and $O+CO^* \rightarrow CO_2 + *$ (L-R2). The base chemistry set, without L-R reactions (red line), is expanded with L-R1 (blue line), or both L-R1 and L-R2 (green lines). The activation enthalpy (E_a) of L-R2 is varied from 0.00 to 0.20 eV (light to dark green). Conditions: T = 500 K, p = 5 mbar and flow rate = 100 sccm

binding catalysts at relatively low temperature (500 K), as CO desorption will improve at higher temperatures (see Sect. "Effect of temperature on plasma-catalytic CO2 splitting" for the effect of temperature for different transition metals).

This effect raises the question whether adsorbed CO* molecules can also efficiently react with incoming O atoms via an L-R reaction, as this would significantly improve the activ-

ity of strong binding catalysts. Nevertheless, to the best of our knowledge, there are no rate coefficients available for this reaction on transition metal surfaces. Yet, we can expect that the L-R reaction of O with adsorbed CO* is more difficult than with O*, as the former requires the O atom to attack the C of CO*, which is directed to the surface and thus shielded by the rest of the CO* molecule.

To illustrate the potential effect of the reaction $O + CO^* \rightarrow CO_2 + *$, we include it in the simulations for Fig. 3 (green curves), in which this reaction is labeled as L-R2. As discussed in the subsection on Langmuir-Rideal reactions in Sect. "Rate coefficients for transition metals", we set the entropy barrier of this reaction equal to the loss of the translational entropy of the incoming O atom, due to the high constraints associated with attacking the C of CO*. The enthalpy of activation is varied from 0.00 to 0.20 eV (corresponding to the light to dark green curves, respectively). In this way, we illustrate the potential effect of L-R2 on the O and O_2 fractions, depending on how facile the reaction can occur.

As shown in Fig. 3 (a), the recombination of O atoms improves when L-R2 is allowed to occur in addition to L-R1. As is evident from the green curves, a lower activation barrier for L-R2 further enhances the recombination of O atoms on the surface and thus reduces the O fraction in the afterglow. Interestingly, the faster drop of the O atom fraction in Fig. 3 (a) also corresponds to a faster rise of the O_2 fraction in Fig. 3 (b). This is caused by the improved removal of CO* molecules from the surface as the barrier for L-R2 drops, and thus the recombination of CO* with O becomes easier. As this reduces the CO* poisoning of the surface, it leads to more free sites on which O atoms can adsorb, which in turn enhances the recombination of O with O* to O_2 (i.e., L-R1). Hence, allowing O atoms to recombine with adsorbed CO* can also improve the recombination between O and O*, by lowering surface poisoning. Nevertheless, the maximum O_2 fraction in Fig. 3 (b) becomes slightly lower upon lowering the activation energy for L-R2, due to more O atoms recombining with CO*, rather than with O*. This is also visible in Fig. 3 (c), as the curves that correspond to the lowest barriers for L-R2 result in the lowest CO mole fractions. Note that the red and blue curves in Fig. 3 (c) overlap, as no CO is consumed on the Rh surface when L-R2 is not considered.

Additionally, the maxima in the O_2 curves (Fig. 3 (b)) are followed by a consistent drop of the O_2 fraction. This is because thermal-catalytic CO oxidation (i.e., oxidation by O* originating from the dissociative adsorption of O_2), becomes the main surface reaction when O atoms start to get depleted. Indeed, with less remaining plasma-produced O atoms or other plasma species, thermal catalysis becomes the dominant reaction mechanism. This can also be observed in Fig. 3 (c), as the CO mole fraction seems to briefly stabilize when the O atoms in the gas drop, followed by a linear decline of the CO mole fraction once the O atoms approach depletion and thermal catalysis becomes the dominant mechanism for CO oxidation. Note, however, that thermal catalytic CO oxidation in Fig. 3 is only possible due to a small amount of remaining O atoms in the gas phase, which avoids that the Rh surface becomes fully poisoned by O* (from O_2) or CO*. If the O atoms are fully depleted, the Rh surface only becomes active for thermal catalytic CO oxidation at temperatures above 900 K, as we will discuss in Sect. "Rh and Pd surfaces".

As CO oxidation produces CO_2, the mole fraction of CO_2 behaves opposite to that of CO, i.e., the CO_2 mole fraction rises as that of CO drops and vice versa, and is therefore not included in Fig. 3. Since CO_2 is thermodynamically favored over CO and O_2 at the conditions of temperature and pressure under study (500 K, 5 mbar), the Rh surface will catalyze

the oxidation of CO to CO_2 which consumes the O_2 formed in the first part of the reactor. This illustrates that the presence of a catalyst material in plasma catalysis (either in- or post-plasma) does not necessarily have a positive effect on the CO_2 conversion, but that the effect of the catalyst can differ, depending on the reaction conditions and the stage of the reaction.

To gain a better understanding of whether a catalyst will have a positive or negative effect on the global reaction, we will study how different transition metal catalysts (Ag, Cu, Pd and Rh) perform relative to each other and a glass surface, for different conditions of temperature, pressure and residence time in the next sections. Note that due to the uncertainty (i.e., lack of a rate coefficient) for the L-R reaction between O and CO* (L-R2), we will exclude this reaction from the chemistry sets of the transition metals in the rest of the paper. This choice is justified, as this reaction is likely difficult because the O atom would have to attack the C atom of CO*, which is directed towards the surface. Also, it will mainly have an impact on conditions that are sensitive to CO* poisoning, namely for catalysts that bind CO* strongly (i.e., Pd and Rh) at low temperature (500 K). However, we do include the recombination of O atoms through L-R (L-R1) in all subsequent simulations, as we illustrated the importance of this reaction in Sect. "Importance of Langmuir-Rideal reactions for O atom recombination".

The Mechanism of low-pressure plasma-catalytic CO_2 Splitting

In this section, we provide insight into the reaction kinetics of CO_2 splitting in a low-pressure plasma and its afterglow exposed to a non-catalytic (glass) or catalytic (Ag) surface, for a single set of (representative) conditions (namely 1100 K, 5 mbar and 100 sccm). Hence, we first discuss the reaction mechanisms at play, providing a basis for the next sections where we discuss how different reaction parameters (catalyst, temperature, pressure and flow rate) affect the kinetics and thus the product yield.

Figure 4 shows the main loss and formation reactions of CO_2 (a), O atoms (b), CO (c) and O_2 (d) in the plasma (first CSTR unit). Destruction of CO_2 happens predominantly via electron impact dissociation into CO and $O(^1D)$, and to a lesser extent via dissociative attachment, as well as dissociation upon collision with $CO(A^3P)$. The main mechanism for CO_2 formation (i.e., back-reactions) is via an L-R reaction between CO and a chemisorbed O atom (O*) (Fig. 4(a)). Likewise, chemisorption is the main loss reaction for O atoms in the plasma, next to electron impact excitation to $O(^1D)$ and the L-R reaction with a chemisorbed O* atom to form O_2 (Fig. 4(b)). Note, however, that most of the $O(^1D)$ formed via electron impact dissociation of CO_2 or excitation of ground-state O, undergoes de-excitation by collisions with CO_2 to again form ground-state O atoms. This is also the main reaction for the formation of ground-state O atoms. Other important O formation reactions are electron detachment from O^- and CO_2 dissociation upon collision with $CO(A^3P)$. The main loss reactions of CO (Fig. 4(c)) are the back-reaction to CO_2 via L-R with a chemisorbed O* atom, as well as electron impact excitation to $CO(A^3P)$. The main formation process of CO is electron impact dissociation of CO_2, followed by dissociative attachment of CO_2, de-excitation of $CO(A^3P)$, as well as, CO_2 dissociation upon collision with $CO(A^3P)$. Lastly, O_2 is formed via L-R between gaseous and chemisorbed O atoms, while a small amount of the formed O_2 is destroyed via electron impact dissociation (Fig. 4(d)).

To summarize, CO_2 dissociates in the plasma, which occurs predominantly via electron impact dissociation to CO and $O(^1D)$. The latter species de-excites to form ground-state O

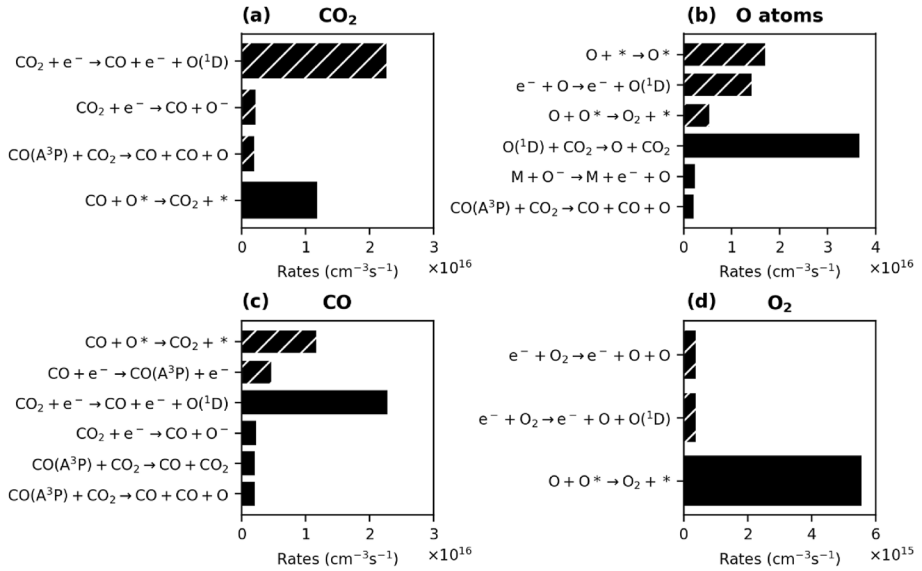

Fig. 4 The main loss (hatched bars) and formation (full bars) reactions and their corresponding rates for CO_2 (**a**), O atoms (**b**), CO (**c**), and O_2 (**d**) in the plasma. Conditions: T = 1100 K, p = 5 mbar and flow rate = 100 sccm

atoms, which adsorb on the chemisorption sites of the glass surface that encloses the plasma. The chemisorbed O* atoms are then either converted back to CO_2 via an L-R reaction with an impinging CO molecule, or they form O_2 via L-R with an impinging O atom.

Figure 5 presents the calculated mole fractions of gas species (a), fractional surface coverages (b), O atom loss rates (c) and net surface rates (d) for a CO_2 plasma afterglow in contact with a (non-catalytic) glass surface. Figure 5 (a) displays the mole fractions of the main gas species except for CO_2, which makes up most of the gas phase. As can be seen, the mole fraction of O drops in the afterglow, as O atoms chemisorb on the glass surface and recombine with incoming CO molecules or other O atoms to form CO_2 or O_2, respectively. Consequently, the CO fraction drops as well, and the O_2 fraction rises, until the O atoms are depleted.

While the chemisorption sites are initially mostly covered with O* atoms, the depletion of O atoms in the gas phase causes a similar decline in the coverage of chemisorbed O* atoms (O^*_c; Fig. 5 (b)). Note that the fraction of physisorbed O atoms (O^*_p) is extremely low and the physisorption sites are almost empty. This is due to the high temperature (1100 K) considered here, as desorption of the weakly bound physisorbed O* atoms occurs very easily. However, even at 500 K most of the physisorption sites are still empty.

Figure 5 (c) displays the total net loss rate of O atoms on the glass surface (red curve), as well as the maximum rate for diffusion of O atoms from the bulk gas to the reactor walls (dashed grey line). As can be seen, the net loss rate for O atoms on the surface is well below the diffusion limit, hence the loss of O atoms is not limited by diffusion. Note that at the low-pressure conditions used in this work (0.5–10 mbar) the loss of O atoms due to gas reactions is negligible compared to recombination on the surface. To illustrate this, the rates of

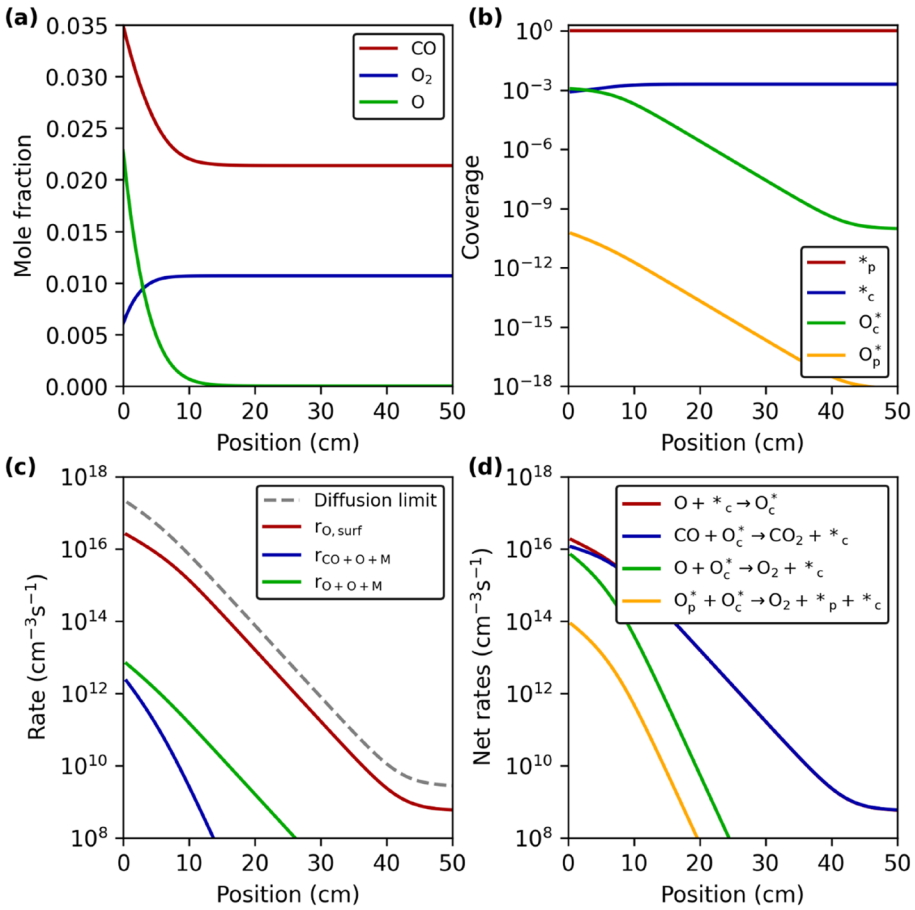

Fig. 5 Mole fractions (**a**), fractional surface coverages (**b**), O atom loss rates (**c**), and net surface rates (**d**) of a CO_2 plasma afterglow in contact with a glass surface. $*_p$, $*_c$, $O*_p$ and $O*_c$ in (**b**) and (**d**) represent empty surface sites for physisorption/chemisorption, and physisorbed/chemisorbed O atoms, respectively. Conditions: T = 1100 K, p = 5 mbar and flow rate = 100 sccm

three-body recombination of O atoms, with either O or CO, to O_2 and CO_2 are also plotted in Fig. 5 (c).

Finally, the net rates of the main surface reactions are plotted in Fig. 5 (d). The main surface pathways on the glass surface involve chemisorption of O atoms, followed by their recombination with either incoming CO or O atoms, via L-R reactions. Right after the plasma, when a significant amount of O is still present in the gas phase, the rates of the L-R reactions that form CO_2 and O_2 are similar (although the latter is slightly lower), but the rate of the L-R reaction with O atoms drops faster as a function of position in the afterglow, due to O atom depletion. In contrast, the rate of the L-H reaction between physisorbed and chemisorbed O* atoms is about two orders of magnitude lower compared to that of the L-R reactions, due to the low coverage of physisorbed O atoms. The rates of L-R reactions with physisorbed O atoms are even lower and therefore not shown in Fig. 5 (d). The rates of all surface reactions drop as the O atoms in the gas phase become depleted.

In analogy with Figs. 5 and 6 illustrates the calculated mole fractions of gas species (a), fractional surface coverages (b), O atom loss rates (c) and net surface rates (d) for a CO_2 plasma afterglow in contact with a (catalytic) Ag surface. The mole fraction of O atoms now drops much more rapidly at the start of the afterglow, as compared to the glass surface (Fig. 5 (a)), which coincides with a rise of the O_2 fraction; see Fig. 6 (a). Following the depletion of the O atoms, the fractions of both CO and O_2 decrease slowly when moving along the afterglow, due to thermal catalytic CO oxidation.

The coverages on the Ag surface remain relatively stable throughout the afterglow, although the O* coverage shows a drop near the start of the afterglow due to fast depletion of the O atoms in the gas phase (Fig. 6 (b)). However, this drop of the coverage remains limited, as adsorbed O* is formed via adsorption and subsequent dissociation of O_2, once O in the gas phase is depleted. Also note that the majority of the surface is empty, which is a consequence of the high temperature and the weakly binding character of Ag. However, the surface coverages for the other, more strongly binding metals considered in this work are

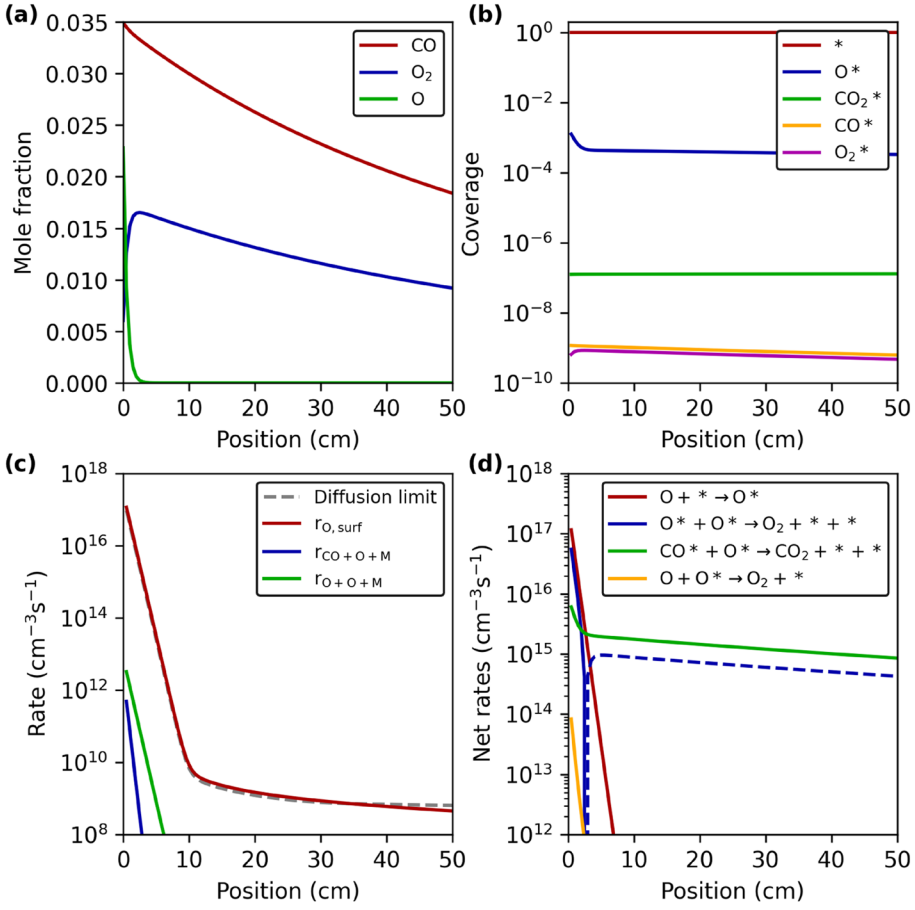

Fig. 6 Mole fractions (**a**), fractional surface coverages (**b**), O atom loss rates (**c**), and net surface rates (**d**) of a CO_2 plasma afterglow in contact with an Ag surface. The dashed line in (**d**) indicates a negative rate. Conditions: T = 1100 K, p = 5 mbar and flow rate = 100 sccm

clearly higher. For reference, the O* coverages are between 0.39 and 0.98 for Cu, between 0.026 and 0.47 for Pd, and above 0.98 for Rh, when using the same reaction conditions as those in Fig. 6.

As can be seen in Fig. 6 (c), the net loss rate of O atoms on the surface becomes limited by diffusion in this case, due to the fast recombination of O atoms on the Ag surface, i.e. the red and the dashed grey curves overlap. Also note again that due to the low-pressure conditions O atom recombination in the gas phase is substantially slower compared to on the surface.

Finally, Fig. 6 (d) shows the net rates of the reactions on the Ag surface. Near the start of the afterglow, when O atoms are still present in the gas phase, the main surface pathway is O atom adsorption and recombination to O_2 via L-H (hence, between adsorbed O*). Recombination between adsorbed O* and CO* into CO_2 is not favored, due to the low CO* coverage at 1100 K. However, as the temperature decreases, the contribution of CO_2 formation, relative to O_2 formation will increase. Likewise, the contribution of O_2 formation via L-R (hence, with incoming O atoms) is negligible for Ag at 1100 K, but will be more important for more strongly binding catalysts and lower temperatures; see next sections. Hence, at high temperatures, the rate of the L-H reaction exceeds that of the L-R reactions, despite the lower O* coverages at high temperatures, as the rate coefficient of the L-H reaction rises more strongly with temperature between 500 and 1100 K relative to that of the L-R reaction. Importantly, following the depletion of the O atoms in the gas phase, the rate of O adsorption drops and O_2* starts dissociating into O* instead. This is indicated by the dashed blue line in Fig. 6 (d), which represents a negative value for this rate (i.e., the reaction proceeds to the left). The O* formed by dissociation of O_2* subsequently oxidizes adsorbed CO* into CO_2 (green line). To summarize, O atoms adsorb on the Ag surface and recombine via a L-H reaction to form O_2. However, once the O atoms in the gas phase are depleted, thermal catalytic CO oxidation will occur, which again forms CO_2, thereby reducing the overall CO_2 conversion.

Note that the enthalpy correction and entropy of the surface species are calculated using the harmonic oscillator approximation, as discussed in Sect. "Rate coefficients for transition metals". To investigate the impact of this assumption, we also simulated the conditions used in Fig. 6 with the free translator approximation, in which surface species are assumed to retain two translational degrees of freedom (i.e., free translation over the surface along two dimensions). We find that if the free translator approximation is used, the rate of thermal-catalytic CO oxidation rises, due to stronger increase in entropy upon dissociation of O_2* into O*, which enhances the dissociation rate. This results in a faster drop of the O_2 and CO mole fractions in the plasma, compared to when the harmonic oscillator approximation is used. A detailed discussion of these results is presented in section S8 of the SI.

Effect of Temperature on plasma-catalytic CO_2 Splitting

In this section we will demonstrate how the optimal catalyst for plasma-catalytic CO_2 splitting is affected by the temperature. We consider L-H reactions, as well as O atom recombination via L-R, which has been shown to be important (see Sect. "Importance of Langmuir-Rideal reactions for O atom recombination"), but not the L-R reaction between O atoms and adsorbed CO*, for the reasons explained above.

Figure 7 shows the mole fractions of O_2 and CO in the afterglow of a CO_2 plasma at 500, 800 and 1100 K, and for different transition metal and glass walls. Note that the mole fraction of O atoms in the gas phase is approximately equal to $n_{CO} - 2n_{O2}$ (due to the stoichiometry of CO_2 splitting into CO + O, with the O atoms partially recombining into ½ O_2), while the remaining part of the gas mixture consists mainly of CO_2. Other plasma species, like ions, electronically excited species, C atoms and O_3, occur only in small amounts and are therefore not relevant for further discussion. The role of the catalyst is thus to reduce recombination between CO and O back to CO_2, by enhancing the recombination of O atoms to O_2.

Note that we compare plasma catalysis with transition metal catalysts, to a plasma and afterglow that are in contact with a glass surface (i.e., the walls of the glass tube surrounding the RF plasma). The latter serves as a reference case for the plasma (afterglow) without catalyst. This is because at the low pressures under study (0.5–10 mbar) the recombination of the plasma species occurs predominantly at the reactor walls, as recombination in the gas phase is very slow. Hence, the formation of O_2 and CO_2 and consumption of O atoms in the bulk gas of the afterglow is negligible compared to the reactions on the surface (except for Pd and Rh at 500 K, which are strongly poisoned, see Sect. "Rh and Pd surfaces"). For reference, if we use the same conditions as in Fig. 7 and neglect surface reactions, the O atom mole fraction drops only slightly: from 3.38×10^{-2} in the plasma to 3.02×10^{-2} at the end of the afterglow at 500 K, and from 5.54×10^{-2} to 5.48×10^{-2} at 1100 K. At 500 K, about 94% of the O atoms that recombine in the bulk gas during their residence time form O_2, while at 1100 K this is about 50%. Hence, at the low-pressure conditions studied in this work, recombination reactions in the gas phase are too slow and therefore not important.

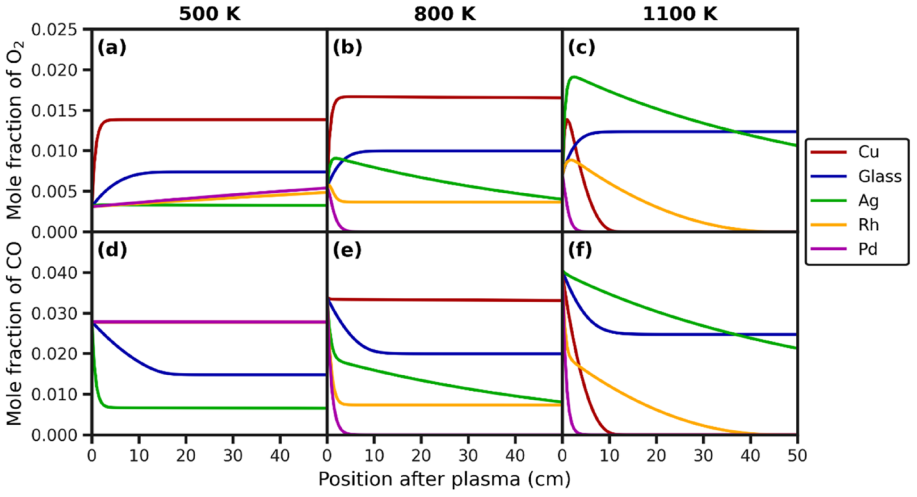

Fig. 7 Evolution of the mole fractions of O_2 (**a**, **b**, **c**) and CO (**d**, **e**, **f**) with position in the afterglow of a CO_2 plasma. The results are plotted for different wall surfaces (transition metals and glass) and temperatures, i.e., 500 K (**a**, **d**), 800 K (**b**, **e**) and 1100 K (**c**, **f**). Other conditions: $p = 5$ mbar and flow rate = 100 sccm

Cu Surface

As can be seen in Fig. 7 (a) and (b), for 500 and 800 K, respectively, Cu gives the highest O_2 fraction of all studied Materials, while at 1100 K, Cu performs significantly worse compared to most other materials (see Fig. 7 (c)). Indeed, at 1100 K the O_2 mole fraction quickly drops in the afterglow, while at lower temperatures the O_2 fraction for the Cu surface initially rises with position and then stays more or less constant (or declines only very slightly). Evidently, the initial rise in O_2 fraction can be explained by the recombination of O atoms on the surface to form O_2. At 500 K (Fig. 7 (a)) the O_2 fraction for Cu remains stable after depletion of the O atoms in the gas phase, as the surface is not thermally active yet. For 800 K (Fig. 7 (b)) the Cu surface starts to become slightly thermally active for CO oxidation, resulting in a very slow decline, which is however difficult to notice in (Fig. 7 (b). As the temperature increases further to 1100 K (Fig. 7 (c)), the Cu surface becomes fully thermally active, resulting in a quick consumption of the O_2 molecules in the afterglow. These effects are also visible in the mole fractions of CO. Figure 7 (d) and (e) show that the CO fraction at 500 and 800 K remains fairly stable, as almost no CO* is oxidized by adsorbed O* radicals or O_2. Note that the curves for Cu and Pd in Fig. 7 (d) overlap. At 1100 K, the higher temperature causes the Cu surface to become fully active for thermal catalysis, resulting in a steep drop of the CO* fraction directly after the plasma, as illustrated in Fig. 7 (f).

Glass Surface

The O_2 fraction for the glass surface at 500 and 800 K (Fig. 7 (a) and (b), respectively) behaves similarly to that of Cu, i.e., the O_2 fraction initially rises due to O atom recombination and remains constant once the O atoms are depleted. However, the glass surface is not active in thermal catalysis (i.e. in the absence of O atoms) and will thus not become thermally active at higher temperatures. Hence, even at 1100 K the O_2 fraction in the gas phase will initially increase and subsequently remain constant; see Fig. 7 (c). Contrary to Cu, however, the glass surface also facilitates recombination between CO and adsorbed O* radicals, even at low temperatures. This results in an initial drop of the CO fraction for the glass surface at all temperatures studied (see Fig. 7 (d), (e) and (f)).

Ag Surface

While Cu is the best performing catalyst at 500 K for producing both O_2 and CO in the CO_2 plasma afterglow, but one of the worst performing at 1100 K, this trend is reversed for Ag. Indeed, Ag gives the lowest O_2 fractions at 500 K (Fig. 7 (a)), yet has the highest O_2 fractions at 1100 K in most of the plasma afterglow (Fig. 7 (c)), compared to the other materials. Only glass outperforms Ag at 1100 K near the end of the reactor. While Ag and Cu are both relatively weakly binding catalysts, Ag is still more weakly binding compared to Cu. Hence the breaking of bonds between adsorbates and the Ag surface and the formation of new bonds between these adsorbates is easier on Ag. Consequently, the Ag surface can more easily form bonds between adsorbed O* atoms and CO* molecules via L-H reactions, which is favored over O atom recombination into O_2 at 500 K, as can be seen in Fig. 7 (a) and (d). Almost no O atom recombination into O_2 occurs for Ag at 500 K, as the O_2 fraction in Fig. 7 (a) remains constant throughout the entire afterglow. On the other hand, the CO

fraction shows a steep decline for Ag, near the start of the afterglow, and remains constant once the O atoms are depleted, as shown in Fig. 7 (d). Indeed, Ag is a weakly binding catalyst and thus requires high temperatures to be able to break the bond in O_2. Therefore, Ag requires the presence of O atoms to be able to oxidize CO at low temperatures, just like it needs high temperatures to become active for thermal-catalytic CO oxidation. However, as the temperature increases, the Ag surface becomes more selective towards O_2, and less towards the back-reaction into CO_2. Indeed, by comparing Fig. 7 (a), (b) and (c) it is clear that the maximum in the curve of the O_2 mole fraction for Ag becomes strongly enhanced at higher temperatures. This is due to the more facile desorption of CO molecules and thus lower CO* coverages with rising temperature. Hence, less O* will recombine with CO* and more will recombine with other O atoms, via either L-H or L-R reactions, as the temperature increases. Moreover, since Ag is more weakly binding than Cu, Ag allows for easier CO* desorption, and has more difficulty breaking the O_2 bond. Thus, at high temperature Ag will be more selective towards O_2 formation and less active for thermal-catalytic CO oxidation compared to other metals, as can be seen at 1100 K in Fig. 7 (c). At both 800 and 1100 K (Fig. 7 (b) and (c)), the curve of the O_2 fraction for Ag shows a clear maximum due to the initial recombination of O atoms into O_2, followed by O_2 consumption via thermal-catalytic CO oxidation. Based on the O_2 fraction at the Maximum, Ag is the best performing catalyst at 1100 K, however thermal catalysis (oxidation of CO into CO_2) causes the O_2 and CO fractions to drop later in the reactor. This illustrates the importance of controlling thermal-catalytic back-reactions that occur in combination with plasma-catalytic CO_2 splitting. This may be possible by limiting the catalytic region in the reactor, or by changing the residence time.

Rh and Pd Surfaces

The results for Rh and Pd at 500 K are similar to each other, i.e., the O_2 fractions for both catalysts rise slowly throughout the reactor due to recombination of O atoms, as shown in Fig. 7 (a). Likewise, the CO fractions of Rh and Pd remain quasi constant at 500 K and the curves for both catalysts overlap, as illustrated in Fig. 7 (d). As we explained in Sect. "Effect of L-R reactions in plasma-catalytic CO2 splitting", the low activity and slow O atom recombination is due to CO* poisoning of these catalysts at 500 K. Whether these results are accurate or not depends on the possibility for O atoms to recombine with adsorbed CO* via an L-R reaction, as also discussed in Sect. "Effect of L-R reactions in plasma-catalytic CO2 splitting". If that reaction is sufficiently easy, CO* poisoning would be avoided, and O atom recombination would be much faster. Nevertheless, at higher temperatures CO* poisoning disappears, regardless of whether L-R between O atoms and CO* is considered, as CO* gains sufficient energy to desorb. Indeed, Pd is highly active for thermal-catalytic CO oxidation at 800 and 1100 K, causing an immediate drop of both the O_2 and CO fractions at the start of the afterglow (Fig. 7 (b, e) and (c, f), respectively).

At 800 K, the Rh surface also catalyzes CO oxidation, causing a drop in the mole fractions of O_2 and CO, see Fig. 7 (b) and (e). However, in contrast with the Pd surface, Rh is not active for thermal catalysis at 800 K, and the consumption of O_2 and CO stops once the O atoms in the gas phase are depleted. This can be explained by the removal of adsorbed O* by incident O atoms via L-R, which opens up free sites on which CO can adsorb. Once the O atoms are depleted, however, the surface is poisoned by adsorbed O*, formed by O_2 dis-

sociative adsorption. This stops further CO oxidation. At 1100 K, Rh behaves similar to Ag, i.e., initially the O_2 fraction rises due to O atom recombination, followed by O_2 consumption through thermal-catalytic CO oxidation (Fig. 7 (c)). However, in contrast with Ag, the Rh surface recombines less O atoms into O_2 and is more selective towards CO oxidation by O atoms. Hence, the maximum in the O_2 fraction is lower and the initial drop in the CO fraction is steeper for Rh compared to Ag (see Fig. 7 (c) and (f) for O_2 and CO, respectively).

Summary

In summary, the optimal catalyst depends both on its activity for O atom recombination into O_2, as well as for thermal catalytic CO oxidation into CO_2. Indeed, Cu performs well at low to intermediate temperatures, as it selectively recombines O atoms into O_2 via L-R reactions, and thus avoids recombination of O atoms with CO back to CO_2. Yet, at high temperatures Cu becomes active for thermal catalytic CO oxidation, causing a drop in the CO and O_2 mole fractions. Conversely, Ag performs very bad at low temperatures, as its weakly binding character enables facile recombination between adsorbed O* atoms and CO* to form CO_2 via the L-H mechanism. Yet, at high temperatures Ag performs very well compared to the other catalysts, as less CO* remains adsorbed on the surface to recombine with O*, and the difficult dissociation of O_2 on Ag results in a relatively low rate for thermal catalytic CO oxidation. Pd is very active for thermal catalytic CO oxidation, except at low temperatures at which it is poisoned by CO*, and thus performs bad for plasma-catalytic CO_2 splitting. Rh is fairly inactive for both O atom recombination into O_2, as well as thermal catalytic CO oxidation. Consequently, Rh generally performs moderately. Lastly, the glass surface gives moderate to good results (especially at high temperatures) as it is not active for thermal catalytic CO oxidation, and only aids in recombination of O atoms with other O atoms or CO.

The Optimal Catalyst Depends on Temperature and Residence time

As discussed above, the best catalyst in terms of O_2 formation can change depending on the position in the reactor. Hence, we can compare catalyst performance based on the O_2 and CO fractions at the reactor outlet, but this is dependent on our choice of reaction conditions and reactor dimensions. As such, the potential of the catalyst for plasma-catalytic CO_2 splitting can also be expressed by the maximum O_2 fraction attained in the reactor. Indeed, the drop in the O_2 fraction due to thermal catalytic CO oxidation may be avoided by limiting the catalytic bed length (or catalytically active region of the reactor wall) or altering the residence time in the catalytic bed. To compare the performance of the different catalyst materials (or glass surface) as a function of temperature, we therefore compare both the O_2 mole fraction at the outlet, as well as the maximum O_2 fraction in the reactor, which are displayed in Fig. 8 (a) and (b), respectively.

Cu Surface

By looking at the curves for Cu in Fig. 8, it becomes clear that Cu is the best performing catalyst at low and intermediate temperatures (500–850 K), both based on the outlet and maximum O_2 fractions. However, the outlet O_2 fraction (Fig. 8 (a)) rapidly drops above

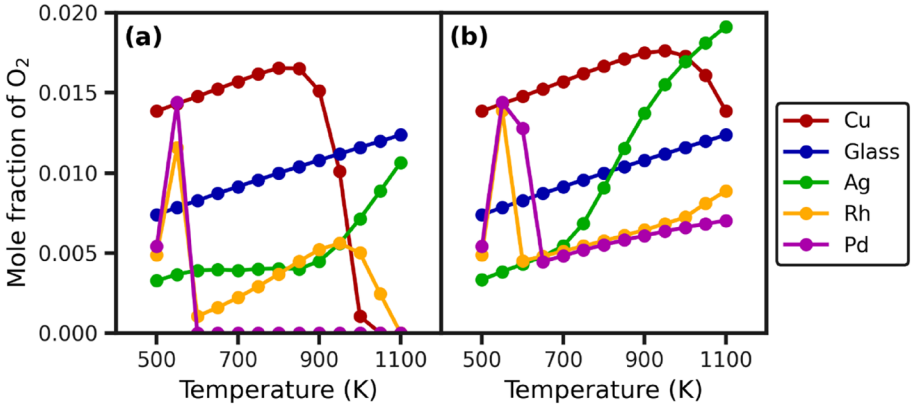

Fig. 8 Influence of temperature on the O_2 mole fraction at the reactor outlet (**a**) and at its maximum in the reactor (**b**), for the different transition metals and the glass surface. Other conditions: $p = 5$ mbar and flow rate = 100 sccm

900 K, as the Cu surface becomes active for thermal-catalytic CO oxidation, while the decline of the maximum O_2 fraction (Fig. 8 (b)) occurs more slowly. Moreover, the highest O_2 fraction in Fig. 8 (b) occurs at a higher temperature (950 K) compared to Fig. 8 (a) (800 K). This indicates that there is still potential for further optimization of the O_2 fraction, and thus CO_2 conversion, at the reactor outlet, by shortening the catalytic region, or reducing the gas residence time (by a shorter catalyst bed or higher flow rates), when working at temperatures above 800 K.

Glass Surface

As observed in Fig. 8, the outlet (a) and maximum (b) O_2 fractions for the glass surface are the same, as glass is not active for thermal catalysis, and thus will not consume O_2 for CO oxidation, regardless of temperature. As such, glass is the best performing surface for CO_2 splitting at high temperatures ($\geq$900 K), when looking at the outlet O_2 fraction in Fig. 8 (a), because the transition metal catalysts will all give rise to thermal-catalytic CO oxidation to CO_2, to some extent. However, when looking at the maximum achievable O_2 fractions in Fig. 8 (b), the glass surface is outperformed by different transition metals at all temperatures, most notably by Ag at high temperatures ($\geq$900 K).

Ag Surface

While Ag results in a high O_2 fraction at high temperature, it is one of the worst performing materials at low temperatures ($\leq$700 K), as it selectively recombines O atoms with CO back to CO_2. Above 700 K, O atom recombination into O_2 also becomes relevant for the Ag surface, which can be observed from the increase in the maximum achievable O_2 fraction in Fig. 8 (b). However, the O_2 fraction at the outlet (Fig. 8 (a)) remains more or less constant for the Ag surface between 700 and 900 K, as O_2 formation by O atom recombination is compensated for by subsequent thermal-catalytic CO oxidation. Note that Ag, being a weakly binding catalyst, can readily catalyze the formation of new bonds (i.e., the

formation of CO_2* from adsorbed CO* and O*) at low temperatures, while it struggles with breaking bonds in molecules, i.e., O_2* dissociation. Hence, when Ag becomes active for thermal catalysis around 700 K, this is the result of the O_2 dissociation step becoming active, while recombination of CO* and O* already occurs at a lower temperature, as O atoms are provided by the plasma. Above 900 K, the O_2 fraction at the reactor outlet also rises (Fig. 8 (a)), as more O_2 is formed near the start of the afterglow than can be consumed by thermal-catalytic back-reactions in the rest of the reactor. Note that this of course depends on the reactor dimensions. Based on the maximum achievable O_2 fraction in Fig. 8 (b), Ag becomes the best performing catalyst above 900 K, outperforming both Cu and glass. As discussed previously, higher temperatures strongly reduce the amount of adsorbed CO* on the weakly binding Ag catalyst, which results in less CO oxidation by adsorbed O atoms. Consequently, more O atoms will recombine with each other into O_2, through L-R or L-H reactions, upon rising temperature.

Rh and Pd Surfaces

The Rh and Pd surfaces behave similarly at low temperatures, as also discussed in Sect. "Rh and Pd surfaces" above. At 500 K, the reactions on both Rh and Pd are strongly limited by CO* poisoning, making the recombination of O atoms into O_2 very slow, as was also visible in Fig. 7 (a). Hence, Fig. 8 (a) and (b) show the same values at 500 K for both the O_2 fraction at the maximum and at the reactor outlet, as the O_2 fraction in the afterglow is still rising with the position in the reactor. At slightly higher temperature (550 K) the O_2 fractions for both Rh and Pd show a peak in Fig. 8 (a) and (b). This is due to a drop in CO* poisoning by the easier CO* desorption at higher temperature. Consequently, more O atoms can adsorb and recombine into O_2 via L-R. However, as the temperature further rises, the O_2 fraction drops as CO oxidation becomes feasible, which can be seen for both the outlet and maximum O_2 fractions in Fig. 8 (a) and (b), respectively. Indeed, Rh and Pd are relatively strongly binding catalysts that struggle with bond formation reactions between adsorbates (L-H mechanism), as these catalysts themselves form strong bonds with the adsorbates. Yet above 600 K the temperature is sufficiently high for CO* and O* to associate into CO_2*, meaning that CO oxidation by adsorbed O atoms or through thermal catalysis can occur. For Pd, the outlet O_2 fraction (Fig. 8 (a)) is near zero for temperatures $\geq$ 600 K, as Pd is a very good catalyst for CO oxidation and will thus quickly revert the gas composition to the thermal equilibrium ($\approx$ 100% CO_2). Indeed, Pd is used as an exhaust catalyst for CO oxidation in the automotive industry [85, 86]. For Rh, the outlet O_2 fractions at temperatures $\geq$ 600 K are larger than for Pd. Indeed, at intermediate temperatures (600–950 K) the Rh surface can only oxidize CO in the presence of O atoms, as shown in Fig. 7 (b). This is because the O atoms free up a part of the surface by removing O* via an L-R reaction, thus allowing for adsorption and oxidation of CO. As the temperature rises from 600 to 950 K, the outlet O_2 fraction in Fig. 8 (a) increases, as CO* desorbs more easily, and thus less CO oxidation will occur. Above 950 K, the outlet O_2 fraction drops as the rate of thermal-catalytic CO oxidation by O_2 increases. When looking at the maximum achievable O_2 fractions (Fig. 8 (b)), the results for Pd and Rh are almost identical in the temperature range between 650 and 900 K, as the maximum O_2 fraction is at the start of the afterglow. Indeed, as the reaction proceeds, O_2 will be consumed by CO oxidation. However, at temperatures above 900 K, the maxi-

mum O_2 fraction for Rh increases slightly relative to that of Pd, as the Rh surface becomes more notably active for O atom recombination into O_2.

Summary

There is still potential for improving the CO and O_2 yields at the outlet by avoiding thermal catalytic CO oxidation, which could be achieved by tuning the residence time or limiting the length of the catalyst bed. Especially for Ag above 600 K, there is a clear difference between the maximum and outlet O_2 fractions, due to thermal catalytic CO oxidation (by O_2) after the O atoms in the gas phase are depleted. Based on the maximum O_2 fraction in the reactor, Ag could become the best performing catalyst above 1000 K, while for our current set of reaction parameters the glass surface gives the highest outlet O_2 fraction. Nevertheless, below 950 K the best performing catalyst is always Cu, both based on the maximum and outlet O_2 fractions. Pd is by far the worst performing catalyst at temperatures above 600 K, both based on the maximum and outlet O_2 fractions, while Rh performs slightly better. However, both Rh and Pd show a narrow spike in maximum and outlet O_2 fraction around 550 K.

Effect of Pressure on plasma-catalytic CO_2 Splitting

In this section, we illustrate how plasma-catalytic CO_2 splitting is affected by the gas pressure. As we find that the effect of pressure is similar for all surfaces and temperatures under study, we discuss the results of one transition metal as a general example. We choose the Cu surface at 1100 K, as the evolution of the O_2 and CO mole fractions with position in the afterglow is the clearest (i.e., steepest) for this catalyst. Figure 9 (a) and (b) therefore display the evolution of the O_2 and CO mole fractions, respectively, with position in the afterglow for the aforementioned conditions (Cu, 1100 K), and pressures varying from 0.5 to 10.0 mbar. Additionally, we list the mole fractions of the main gas species at the end of the plasma (i.e., the first point in Fig. 9) in Table 3 for the different pressures.

As can be seen in Fig. 9, lower pressures result in higher maximum O_2 and CO fractions, while their subsequent decline due to thermal-catalytic back-reactions is slower, thus resulting in higher O_2 and CO mole fractions in the entire afterglow.

The reason for this is twofold: first, higher pressures result in a different EEDF, because there are more electron-neutral collisions, leading to lower electron energies and thus less electron impact ionization. Indeed, we find that the electron density in the plasma region is lower at 10.0 mbar ($n_e = 2.6 \times 10^{10}$ cm^{-3}), compared to 0.5 mbar ($n_e = 2.5 \times 10^{11}$ cm^{-3}). Hence, the lower electron energy and density at higher pressure hinder the formation of O atoms via electron impact dissociation of CO_2. Consequently, the O and CO densities do not rise proportionally with increasing pressure, resulting in lower O and CO fractions at the end of the plasma for higher pressures, as can be seen in Table 3. Thus, due to the lower mole fraction of O atoms available for recombination, a lower fraction of O_2 is formed.

In addition, less of the available O atoms will recombine into O_2 at higher pressures and more will react back to CO_2. Indeed, while the CO mole fraction in the plasma is lower at higher pressures, i.e. 0.021 at 10 mbar vs. 0.15 at 0.5 mbar, this is not the case for the CO number density, which equals 1.4×10^{15} cm^{-3} at 10 mbar vs. 5.0×10^{14} cm^{-3} at 0.5 mbar. Hence, the CO density rises with pressure, albeit by a lower factor than the pressure itself.

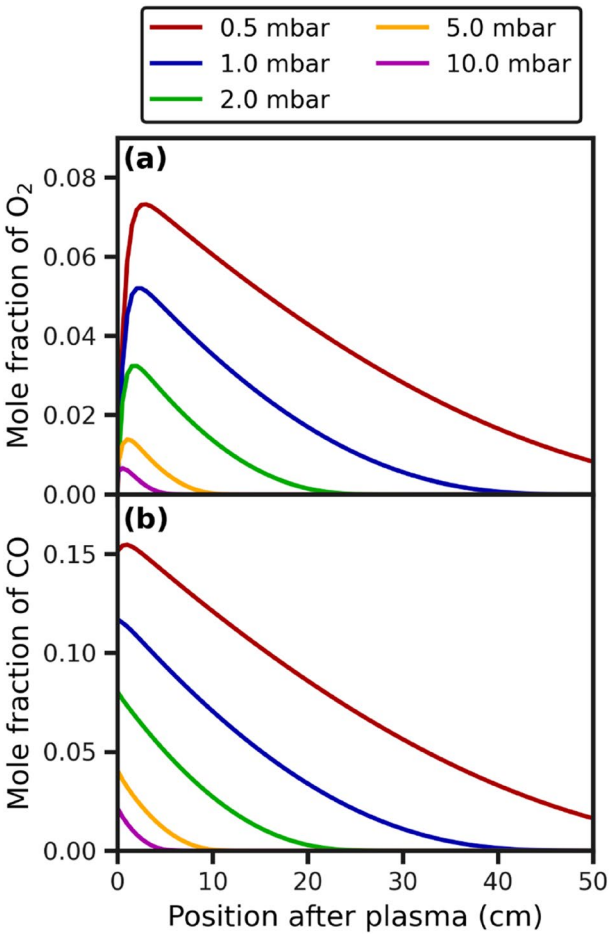

Fig. 9 Effect of pressure on the spatial evolution of the O_2 (**a**) and CO (**b**) mole fractions in the afterglow for a Cu surface. Other conditions: T = 1100 K and flow rate = 100 sccm

Table 3 Mole fractions of the Main gas species at the end of the plasma for different pressures at 1100 K and 100 Sccm

Pressure (mbar)	O_2 Mole fraction	CO Mole fraction	O Mole fraction	CO_2 Mole fraction
0.5	1.9×10^{-3}	1.5×10^{-1}	1.5×10^{-1}	6.9×10^{-1}
1.0	3.4×10^{-3}	1.2×10^{-1}	1.1×10^{-1}	7.7×10^{-1}
2.0	5.7×10^{-3}	8.0×10^{-2}	6.9×10^{-2}	8.5×10^{-1}
5.0	7.0×10^{-3}	4.0×10^{-2}	2.6×10^{-2}	9.3×10^{-1}
10.0	5.7×10^{-3}	2.1×10^{-2}	9.9×10^{-3}	9.6×10^{-1}

The higher CO density at higher pressures enhances the CO adsorption and oxidation on the catalyst surface, which results in more O atoms reacting back to CO_2. This is also visible in Fig. 9 (a), in which the initial rise in O_2 fraction becomes smaller upon rising pressure.

In summary, our results show that plasma-catalytic CO_2 splitting would benefit from operating at lower pressures, at least within the pressure range under study (0.5 to 10 mbar). This effect is partly due to the physical changes in the plasma (lower electron energy and

density at higher pressure) and partly due to catalytic effects (CO oxidation at the catalyst surface). The use of lower gas pressures enhances the O_2 mole fraction and consequently allows for more facile tuning of residence time and length of the catalyst bed, as higher O_2 fractions will be available in a broader region of the reactor. Note, however, that for temperatures at which the catalyst is not thermally active, the O_2 fraction will stop changing when the O atoms in the afterglow are depleted, regardless of the pressure used. Also note that for all pressures in Fig. 9, the simulations are performed with a flow rate of 100 sccm and a plasma power of 100 W, and thus all correspond to the same specific energy input (SEI), namely 13.8 eV/molecule. Finally, it should be kept in mind that in practice, plasma catalysis is more feasible at atmospheric pressure. However, our results are useful to obtain better insights in the current limitations, and how to overcome them, by tuning various operating conditions.

Effect of Flow Rate on plasma-catalytic CO_2 Splitting

To illustrate the influence of the flow rate in plasma-catalytic CO_2 splitting, we plot the O_2 and CO mole fractions in the afterglow, in Fig. 10 (a) and (b), respectively, at different flow rates and for both Ag and glass surfaces. Hence, we show results for a (thermally active) catalytic surface (Ag), and a non-catalytic surface (glass). Additionally, we list the mole fractions of the main gas species at the end of the plasma in Table 4 for the different flow rates. In case of the Ag surface, the effect of lowering the flow rate is two-fold: on one hand, the maximum O_2 fraction (Fig. 10 (a)) increases, but on the other hand, the subsequent drop in O_2 fraction occurs much faster. Indeed, by lowering the flow rate, the residence time becomes longer, and the SEI rises. Consequently, more CO_2 molecules dissociate in the plasma, resulting in more O atoms which recombine into O_2, thus leading to higher maximum O_2 fractions, as can be seen in Table 4. However, the formed O_2 molecules also take longer to travel through the reactor at lower flow rates, resulting in more O_2 consumption by thermal-catalytic CO oxidation, and thus, a steeper decline of the O_2 fraction with the position in the afterglow. Likewise, the CO mole fractions (Fig. 10 (b)) at the start of the afterglow are higher for lower flow rates, but also drop more quickly with position in the reactor. This second effect does not occur on the glass surface, because it is not catalytically active. Hence, lower flow rates are always beneficial in the case of the non-catalytic glass surface, while for the catalytic Ag surface the effect can be either positive or negative, depending on the position in the reactor.

As such, the length of the post-plasma-catalytic bed should ideally be tuned against the flow rate, if the transition metal is catalytic and thermally active at the operating temperature. Indeed, by limiting the catalytic region to the space in the reactor where O_2 formation occurs, the subsequent destruction of O_2 (and CO) by thermal catalytic CO oxidation can be avoided. In this case, the maximum O_2 fraction would also be the outlet O_2 fraction, and the use of Ag and low flow rates would be favored over a glass surface and high flow rates. As can be seen in Fig. 10, the maximum O_2 fraction for Ag exceeds that of glass at all flow rates, and the highest maximum is attained for the lowest flow rate. However, when comparing the O_2 and CO fractions at the outlet (50 cm) in Fig. 10 (a) and (b), the Ag surface only outperforms the glass surface at the highest flow rate (200 sccm). At lower flow rates, the O_2 and CO fractions for the Ag surface drop below that for glass, due to the enhanced O_2 and CO consumption. Hence, the best catalyst material for attaining high O_2 and CO frac-

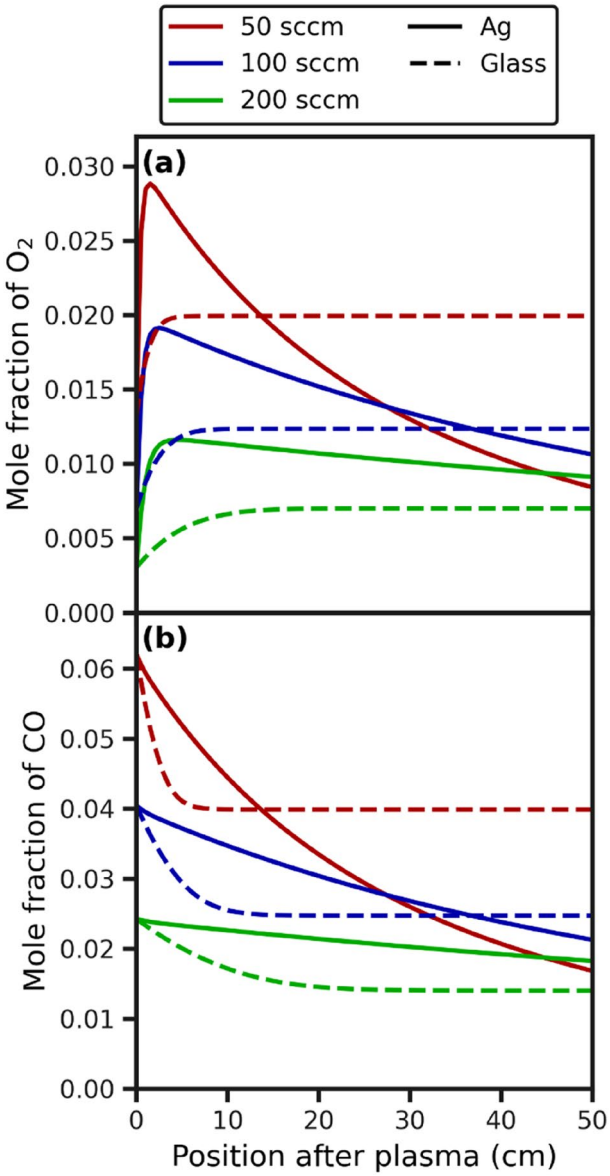

Fig. 10 Effect of the flow rate on the spatial evolution of the O_2 (**a**) and CO (**b**) mole fractions in the afterglow, for Ag (full lines) and glass (dashed lines) surfaces. Other conditions: T = 1100 K and p = 5 mbar

Table 4 Mole fractions of the Main gas species at the end of the plasma for different flow rates at 1100 K and 5 Mbar

Flow rate (sccm)	O_2 Mole fraction	CO Mole fraction	O Mole fraction	CO_2 Mole fraction
50	1.3×10^{-2}	6.2×10^{-2}	3.5×10^{-2}	8.9×10^{-1}
100	7.0×10^{-3}	4.0×10^{-2}	2.6×10^{-2}	9.3×10^{-1}
200	3.1×10^{-3}	2.4×10^{-2}	1.8×10^{-2}	9.5×10^{-1}

tions (and thus a high CO_2 conversion) can differ depending on the flow rate. Moreover, for thermally active catalysts, such as Ag in Fig. 10, there exists an optimum between high and low flow rates, as the highest outlet O_2 and CO fractions for Ag are attained at 100 sccm, while both 50 and 200 sccm result in less O_2 and CO at the outlet.

Finally, we consider how the effect of the flow rate translates to other catalyst materials and conditions. If the catalyst surface is not thermally active at the operating temperature, the gas composition will stop changing once the radicals in the afterglow are depleted. Consequently, the CO_2 dissociation in the plasma, and thus also the formation of O_2 and CO, will always rise upon lowering the flow rate (as explained above, hence independent of the surface material after the plasma), while no subsequent thermal-catalytic back-reactions occur. Hence, under these conditions, a lower flow rate will always result in higher O_2 and CO fractions, and thus a higher CO_2 conversion, at the reactor outlet. This is always the case for glass, but also for transition metals that are not thermally active at the operating temperature. For example, in Fig. 7 (b) the O_2 fraction for the Rh surface at 800 K stabilizes at a non-zero value after depletion of the O atoms in the plasma, and similarly, the O_2 content for Cu at 800 K drops only very slowly. Hence, the net O_2 formation for Rh and Cu surfaces at 800 K will mainly benefit from a lower flow rate, as this will primarily enhance the number of O atoms formed in the plasma. However, if the catalyst is thermally active at the operating temperature, the initial rise in O_2 fraction is followed by a drop due to thermal-catalytic CO oxidation. Consequently, there is an optimal flow rate that balances the effects of the higher CO_2 dissociation at lower flow rates against the reduced O_2 consumption at higher flow rates. Note that for some catalysts the consumption of O_2 occurs directly at the start of the afterglow, before depletion of the O atoms. In this case, the maximum O_2 fraction coincides with that in the plasma and will thus rise for lower flow rates, while the subsequent decline of the O_2 fraction will still become more rapid upon lower flow rate.

In summary, lower flow rates, and thus higher SEI's, result in more CO_2 dissociation in the plasma, but also increase the residence time in the catalyst bed. If the catalyst is thermally active for CO oxidation, the longer residence time causes more CO and O_2 to react back to CO_2. Hence, the optimal flow rate depends on the catalyst and its activity for CO oxidation.

Discussion of the Optimal Catalyst Properties

Finally, in this section, we discuss which properties should be targeted when searching for the optimal catalyst for plasma-catalytic CO_2 splitting, based on our modelling insights. For the conditions under study, the role of the plasma is to activate the CO_2 molecules, i.e., by electron impact dissociation. Hence, the plasma causes a departure from the thermodynamic equilibrium composition (which favors CO_2 at these conditions) resulting in the formation of O atoms and CO molecules. The role of the catalyst is then to minimize the recombination of O with CO back into CO_2, by maximizing the recombination of O atoms into O_2. However, the catalyst should not be (too) active for thermal catalysis under the envisioned reaction conditions, as this will cause a return to the thermodynamic equilibrium composition (i.e., pure CO_2), due to thermal catalytic CO oxidation.

To avoid back-reactions to CO_2, the catalyst should preferentially have a high activation barrier for recombination between adsorbed CO* and O*, while a low CO* coverage and thus a low CO* binding strength is also preferred. However, in practice the adsorption ener-

gies of adsorbates and the activation barriers for reactions between adsorbates cannot be varied independently. This is due to existence of Brønsted-Evans-Polanyi (BEP) relations, i.e. correlations between reaction and activation energies, as well as linear scaling relations between the binding strength of different adsorbates, in heterogenous catalysis [87, 88]. Therefore, catalysts that bind adsorbates weakly have lower activation barriers for their desorption and recombination reactions. As such, low CO* binding strengths result in lower barriers for CO_2 formation, but also more facile CO* desorption. Hence, there should exist an optimal CO* binding strength at which these conflicting effects are balanced. Our model predicts that for the system and conditions under study, the catalysts that bind CO* weakly, i.e. Ag and Cu ($\Delta H^\circ_{CO(g)\rightarrow CO*} = -0.17$ eV and -0.61 eV, respectively), generally perform better than catalysts that bind CO* strongly, i.e. Pd and Rh ($\Delta H^\circ_{CO(g)\rightarrow CO*} = -1.76$ eV and -1.74 eV, respectively). Indeed, adsorbed CO* can only be removed from the surface via desorption or recombination to CO_2. If both are difficult, the surface will become poisoned by CO*, which we find to be the case for Pd and Rh at 500 K and 5 mbar. Thus, our model reveals that the optimal catalyst binds CO* weakly, i.e., has a larger, less negative CO adsorption enthalpy, to allow for facile CO* desorption.

However, a weak CO* binding not only promotes desorption, but also recombination of CO* with O* to form CO_2. To compensate for this effect and retain a sufficiently high activation barrier for CO_2 formation, a catalyst that binds O* strongly might be desired. Indeed, stronger O* binding stabilizes adsorbed O* atoms, and thus results in higher activation barriers for reactions involving O*, such as the reaction with CO* to form CO_2. In other words, if the catalyst binds both O* and CO* weakly, they are not stabilized as much and the barrier for CO_2 formation will be low. This is the case for Ag, which binds both CO* and O* weakly ($\Delta H^\circ_{CO(g)\rightarrow CO*} = -0.17$ eV and $\Delta H^\circ_{0.5O2(g)\rightarrow O*} = -0.64$ eV). Indeed, Ag efficiently catalyzes the recombination of O* and CO* to CO_2 at relatively low temperatures (500–700 K). Nevertheless, as the temperature rises, the contribution of CO* desorption relative to recombination increases, as desorption is an entropically driven process, and Ag becomes a good catalyst for O* recombination to O_2. Cu, on the other hand, binds CO* relatively weakly ($\Delta H^\circ_{CO(g)\rightarrow CO*} = -0.61$ eV), but O* quite strongly ($\Delta H^\circ_{0.5O2(g)\rightarrow O*} = -1.78$ eV). Indeed, the O* binding strength of Cu lays in between Pd ($\Delta H^\circ_{0.5O2(g)\rightarrow O*} = -1.47$ eV), and Rh ($\Delta H^\circ_{0.5O2(g)\rightarrow O*} = -2.19$ eV). While the weak CO* binding of Cu improves CO* desorption, the relatively strong O* binding increases the activation barrier for recombination between O* and CO*, thus limiting CO_2 formation. However, the stronger O* binding also results in more difficult recombination of O* atoms to O_2 and more facile dissociation of O_2 to O* atoms, as the catalyst stabilizes the surface bound O* more strongly. Yet, the activation barrier for O atom recombination via L-R does not increase much with rising O* binding strength, so that O_2 formation via L-R remains facile as long as O atoms are present in the gas phase. As such, we find that Cu is a good catalyst for O atom recombination at temperatures between 500 and 900 K. Yet, at higher temperatures, Cu starts to dissociate the formed O_2 and becomes active for thermal catalytic CO oxidation to CO_2. It is important to note that stronger O* binding results in more facile O_2 dissociation and hence in a lower temperature needed for thermal catalytic CO oxidation by O_2, that is, as long as O_2 dissociation is the rate-limiting step. Because of this, Ag becomes a better catalyst for O recombination to O_2 than Cu at high temperatures.

As discussed in Sect. "Effect of L-R reactions in plasma-catalytic CO2 splitting", it may be possible that CO_2 can also be formed by L-R reactions between adsorbed CO* and an

impinging O atom from the gas phase. While we did not consider this reaction in the rest of the paper, due to its many uncertainties, we would like to note that the reaction would benefit from high CO* coverages. Thus, to counteract it, high O* and low CO* coverages would be needed, which means that catalysts that bind O* strongly and CO* weakly are still preferred.

To conclude, catalysts that bind CO* weakly are expected to be promising candidates for plasma-catalytic CO_2 splitting, while the optimal O* binding strength may vary depending on the temperature. Overall, materials that bind O* strongly, such as Cu, are expected to be better at lower temperatures, yet might more quickly become active for thermal catalytic CO oxidation as the temperature rises. Higher temperatures might therefore require catalysts that bind O* more weakly, such as Ag.

Conclusion

We developed a new coupled plasma-surface microkinetic model with a Boltzmann solver to study the interaction of plasma-produced radicals and molecules with a transition metal or glass surface placed in the afterglow of a low-pressure CO_2 discharge. We consider four transition metals, namely Ag, Cu, Pd and Rh, as well as glass, which represents the glass tube surrounding the plasma/afterglow, and we compare their effect on the reaction kinetics for plasma-catalytic CO_2 splitting. Moreover, we used DFT to calculate the reaction barriers on the transition metal catalysts and we combine these with TST to acquire surface rate coefficients that are used as input for our model. Although our model could not yet be validated against experimental data, and thus cannot make quantitative predictions, it can still provide qualitative trends, insights and comparisons on the influence of the different catalysts and reactions conditions.

We do not only consider adsorption of radicals on the surface followed by L-H reactions, but also their recombination via L-R reactions. Indeed, based on simulations for a pure O_2 plasma, we suggest that L-R reactions play an important role in O atom recombination on transition metal surfaces, as the high recombination coefficients that are reported in literature for transition metals cannot be explained by our model based on L-H reactions alone, at least for temperatures $\leq$ 600 K.

In plasma-catalytic CO_2 splitting, recombination of O atoms via L-R results in O_2 formation and creates free surface sites, enabling some CO to adsorb next to O atoms. Consequently, some recombination of O and CO back to CO_2 also occurs. However, transition metals also become active for thermal catalytic CO oxidation by the formed O_2 if the temperature is sufficiently high, resulting in a subsequent decline of the O_2 and CO mole fractions, and thus also of the CO_2 conversion, as well as a maximum in the evolution of the O_2 mole fraction vs. position in the reactor. Moreover, the temperature at which a catalyst becomes active for thermal catalytic back-reactions depends strongly on the type of metal. Hence, the optimal catalyst depends strongly on the operating temperature. In other words, there is no single best catalyst, but rather an optimal catalyst for specific reaction conditions.

We find that Cu is the best catalyst up to 900–1000 K, as this relatively weakly binding metal can easily recombine O atoms into O_2 via L-R at low temperature, thus avoiding their recombination with CO into CO_2 again, and leading to a higher CO yield and CO_2 conversion. Yet, Cu becomes thermally active for CO oxidation into CO_2 above 900 K.

The Ag surface, on the other hand, performs very badly at low temperatures, as its very weakly binding character results in low barriers for recombination between adsorbed O* and CO* via L-H, causing most O atoms to react with CO to again form CO_2. However, as the temperature rises, less CO* remains adsorbed on the surface, causing more O atoms to recombine into O_2 and leading to higher maximum O_2 and CO mole fractions in the reactor, and a higher CO_2 conversion. Hence, Ag is the optimal catalyst at very high temperatures (> 1000 K), provided that the length of the catalytic zone is limited to avoid thermal catalytic back-reactions after the O atoms in the gas phase are consumed.

Both Pd and Rh are poisoned by CO* at 500 K, but Pd becomes highly thermally active for CO oxidation at higher temperatures, making it detrimental for CO_2 splitting. Rh, on the other hand, is neither very efficient at recombining O atoms into O_2 or in thermal catalytic CO oxidation.

Next to temperature, we studied the effect of the gas pressure and flow rate, which determines the residence time of the gas in the catalytic bed. We find that plasma-catalytic CO_2 splitting benefits strongly from lower gas pressures, due to more CO_2 dissociation in the plasma and slower thermal catalytic back-reactions in the afterglow. However, this is not beneficial for practical applications, and therefore, plasma catalysis is typically performed at atmospheric pressure, which might thus limit the achievable CO_2 conversion.

Additionally, lower flow rates result in more CO_2 conversion in the plasma, but also cause more thermal catalytic back-reactions in the reactor due to the longer residence time. Hence, under conditions where transition metals are thermally active, the flow rate should be optimized against the length of the catalyst bed to avoid thermal catalytic CO oxidation after depletion of the O atoms in the gas phase, while still achieving sufficient CO_2 dissociation in the plasma. Indeed, if the flow rate is too low, thermal catalysis may consume a large amount of CO and O_2, and the use of a non-catalytic surface (e.g., glass) would be favored instead.

To conclude, this study illustrates how the performance of different transition metals for plasma catalytic CO_2 splitting can change depending on the reaction conditions, and we also compare their performance with a glass tube surrounding the afterglow. Overall, the optimal catalyst depends both on its activity for O atom recombination into O_2, thus avoiding their recombination with CO back into CO_2, as well as its activity for thermal catalytic CO oxidation into CO_2, and the performance thereof is temperature dependent. Moreover, if the catalyst is active for thermal catalytic CO oxidation, this back-reaction can be avoided by optimizing the flow rate or the length of the catalytic bed. These findings should be considered when comparing different catalysts experimentally.

Supplementary Information The online version contains supplementary material available at https://doi.org/10.1007/s11090-025-10599-4.

Acknowledgements This research was supported by the FWO-SBO project PlasMaCatDESIGN (FWO grant ID S001619N), the FWO fellowship of R. Michiels (FWO grant ID 1114921 N), and the European Research Council (ERC) under the European Union's Horizon 2020 research and innovation programme (grant agreement No 810182 – SCOPE ERC Synergy project). The computational resources and services used in this work were provided by the HPC core facility CalcUA of the Universiteit Antwerpen, and VSC (Flemish Supercomputer Center), funded by the Research Foundation - Flanders (FWO) and the Flemish Government.

Author Contributions B.L.: Conceptualization, Construction of the microkinetic model, Microkinetic modelling simulations, Analysis of the results, Preparing the figures, Writing original draft, Writing-review and

editing.R.M.: DFT simulations, Writing original draft, Writing-review and editing.A.B.: Writing original draft, Writing-review and editing, Supervision, Funding acquisition.

Data Availability No datasets were generated or analysed during the current study.

Declarations

Competing Interests The authors declare no competing interests.

References

1. Climate Change (2023) : Synthesis Report. Contribution of Working Groups I, II and III to the Sixth Assessment Report of the Intergovernmental Panel on Climate Change; Lee, H., Romero, J., Eds.; IPCC: Geneva, Switzerland, 2023; pp 35–115. https://doi.org/10.59327/IPCC/AR6-9789291691647
2. Hepburn C, Adlen E, Beddington J, Carter EA, Fuss S, Mac Dowell N, Minx JC, Smith P, Williams CK (2019) The technological and economic prospects for CO_2 utilization and removal. Nature 575:87–97. https://doi.org/10.1038/s41586-019-1681-6
3. Snoeckx R, Bogaerts A (2017) Plasma Technology – a novel solution for CO_2 conversion? Chem Soc Rev 46(19):5805–5863. https://doi.org/10.1039/C6CS00066E
4. Bogaerts A, Tu X, Whitehead JC, Centi G, Lefferts L, Guaitella O, Azzolina-Jury F, Kim H-H, Murphy AB, Schneider WF, Nozaki T, Hicks JC, Rousseau A, Thevenet F, Khacef A, Carreon M (2020) The 2020 plasma catalysis roadmap. J Phys D: Appl Phys 53(44):443001. https://doi.org/10.1088/1361-6463/ab9048
5. Loenders B, Michiels R, Bogaerts A (2023) Is a catalyst always beneficial in plasma catalysis?? Insights from the many physical and chemical interactions. J Energy Chem 85:501–533. https://doi.org/10.1016/j.jechem.2023.06.016
6. Lefferts L (2024) Leveraging expertise in thermal catalysis to understand plasma catalysis. Angew Chem Int Ed 63(10). https://doi.org/10.1002/anie.202305322
7. Bogaerts A, Neyts EC, Guaitella O, Murphy AB (2022) Foundations of plasma catalysis for environmental applications. Plasma Sources Sci Technol 31(5):053002. https://doi.org/10.1088/1361-6595/ac5f8e
8. Neyts EC, Bogaerts A (2014) Understanding plasma catalysis through modelling and Simulation—a review. J Phys D: Appl Phys 47(22):224010. https://doi.org/10.1088/0022-3727/47/22/224010
9. Mehta P, Barboun P, Herrera FA, Kim J, Rumbach P, Go DB, Hicks JC, Schneider WF (2018) Overcoming ammonia synthesis scaling relations with plasma-enabled catalysis. Nat Catal 1(4):269–275. https://doi.org/10.1038/s41929-018-0045-1
10. Mehta P, Barboun PM, Engelmann Y, Go DB, Bogaerts A, Schneider WF, Hicks JC (2020) Plasma-catalytic ammonia synthesis beyond the equilibrium limit. ACS Catal 10(12):6726–6734. https://doi.org/10.1021/acscatal.0c00684
11. Engelmann Y, Mehta P, Neyts EC, Schneider WF, Bogaerts A (2020) Predicted influence of plasma activation on nonoxidative coupling of methane on transition metal catalysts. ACS Sustain Chem Eng 8(15):6043–6054. https://doi.org/10.1021/acssuschemeng.0c00906
12. Engelmann Y, Van 'T, Veer K, Gorbanev Y, Neyts EC, Schneider WF, Bogaerts A (2021) Plasma catalysis for ammonia synthesis: A microkinetic modeling study on the contributions of Eley-Rideal reactions. ACS Sustain Chem Eng 9(39):13151–13163. https://doi.org/10.1021/acssuschemeng.1c02713
13. Prins R (2018) Eley–rideal, the other mechanism. Top Catal 61(9–11):714–721. https://doi.org/10.1007/s11244-018-0948-8
14. Michiels R, Engelmann Y, Bogaerts A (2020) Plasma catalysis for CO_2 hydrogenation: unlocking new pathways toward CH_3OH. J Phys Chem C 124(47):25859–25872. https://doi.org/10.1021/acs.jpcc.0c07632
15. Loenders B, Engelmann Y, Bogaerts A (2021) Plasma-catalytic partial oxidation of methane on Pt(111): a microkinetic study on the role of different plasma species. J Phys Chem C 125(5):2966–2983. https://doi.org/10.1021/acs.jpcc.0c09849
16. Ma H, Schneider WF (2021) Plasma-Catalyst modeling for materials selection: challenges and opportunities in nitrogen oxidation. J Phys D: Appl Phys 54(45):454004. https://doi.org/10.1088/1361-6463/ac1bd1

17. Ma H, Sharma RK, Welzel S, van de Sanden MCM, Tsampas MN, Schneider WF (2022) Observation and rationalization of nitrogen oxidation enabled only by coupled plasma and catalyst. Nat Commun 13(1):402. https://doi.org/10.1038/s41467-021-27912-2
18. Eshtehardi HA, Van 't Veer K, Delplancke M-P, Reniers F, Bogaerts A (2023) Postplasma catalytic model for NO production: revealing the underlying mechanisms to improve the process efficiency. ACS Sustain Chem Eng 11(5):1720–1733. https://doi.org/10.1021/acssuschemeng.2c05665
19. Maitre P-A, Bieniek MS, Kechagiopoulos PN (2022) Plasma-catalysis of nonoxidative methane coupling: a dynamic investigation of plasma and surface microkinetics over Ni(111). J Phys Chem C 126(47):19987–20003. https://doi.org/10.1021/acs.jpcc.2c03503
20. Andersen JA, Christensen JM, Østberg M, Bogaerts A, Jensen AD (2020) Plasma-Catalytic dry reforming of methane: screening of catalytic materials in a coaxial Packed-Bed DBD reactor. Chem Eng J 397(May):125519. https://doi.org/10.1016/j.cej.2020.125519
21. Sentek J, Krawczyk K, Młotek M, Kalczewska M, Kroker T, Kolb T, Schenk A, Gericke K-H, Schmidt-Szałowski K (2010) Plasma-catalytic methane conversion with carbon dioxide in dielectric barrier discharges. Appl Catal B Environ 94(1–2):19–26. https://doi.org/10.1016/j.apcatb.2009.10.016
22. Van Turnhout J, Aceto D, Travert A, Bazin P, Thibault-Starzyk F, Bogaerts A, Azzolina-Jury F (2022) Observation of surface species in Plasma-Catalytic dry reforming of methane in a novel atmospheric pressure dielectric barrier discharge in situ IR cell. Catal Sci Technol 12(22):6676–6686. https://doi.org/10.1039/D2CY00311B
23. Wang A, Harrhy JH, Meng S, He P, Liu L, Song H (2019) Nonthermal Plasma-Catalytic conversion of biogas to liquid chemicals with low coke formation. Energy Convers Manag 191(April):93–101. https://doi.org/10.1016/j.enconman.2019.04.026
24. Wang L, Yi Y, Wu C, Guo H, Tu X (2017) One-step reforming of CO_2 and CH_4 into high-value liquid chemicals and fuels at room temperature by plasma-driven catalysis. Angew Chem Int Ed 56(44):13679–13683. https://doi.org/10.1002/anie.201707131
25. Chemistry WebBook NIST, *NIST Standard Reference Database Number 69*; Linstrom, P. J., Mallard, W. G., Eds.; National Institute of Standards and Technology: Gaithersburg MD, 20899. https://doi.org/10.18434/T4D303
26. Biondo O, Hughes A, van de Steeg A, Maerivoet S, Loenders B, van Rooij G, Bogaerts A (2023) Power concentration determined by thermodynamic properties in complex gas mixtures: the case of plasma-based dry reforming of methane. Plasma Sources Sci Technol 32(4):045001. https://doi.org/10.1088/1361-6595/acc6ec
27. Paul D, Mozetic M, Zaplotnik R, Primc G, Đonlagić D, Vesel AA (2023) Review of recombination coefficients of neutral oxygen atoms for various materials. Mater (Basel) 16(5):1774. https://doi.org/10.3390/ma16051774
28. Jiang T, Mowbray DJ, Dobrin S, Falsig H, Hvolbæk B, Bligaard T, Nørskov JK (2009) Trends in CO oxidation rates for metal nanoparticles and close-packed, stepped, and kinked surfaces. J Phys Chem C 113(24):10548–10553. https://doi.org/10.1021/jp811185g
29. Yan D, Kristoffersen HH, Pedersen JK, Rossmeisl J (2022) Rationally tailoring catalysts for the CO oxidation reaction by using DFT calculations. ACS Catal 12(1):116–125. https://doi.org/10.1021/acscatal.1c04331
30. Nørskov JK, Studt F, Abild-Pedersen F, Bligaard T (2014) Fundamental concepts in heterogeneous catalysis. John Wiley & Sons, Inc., Hoboken, New Jersey
31. Jiang B, Guo H (2019) Dynamics in reactions on metal surfaces: A theoretical perspective. J Chem Phys 150(180901):1–16. https://doi.org/10.1063/1.5096869
32. Guerra V (2007) Analytical model of heterogeneous atomic recombination on silicalike surfaces. IEEE Trans Plasma Sci 35(5):1397–1412. https://doi.org/10.1109/TPS.2007.902028
33. Afonina NE, Gromov VG, Kovalev VL (2002) Investigation of the influence of different heterogeneous recombination mechanisms on the heat fluxes to a catalytic surface in dissociated carbon dioxide. Fluid Dyn 37(1):117–125
34. Marinov D, Teixeira C, Guerra V (2017) Deterministic and Monte Carlo methods for simulation of Plasma-surface interactions. Plasma Process Polym 14(1–2):1–18. https://doi.org/10.1002/ppap.201600175
35. Kresse G, Hafner J (1993) Ab initio molecular dynamics for liquid metals. Phys Rev B 47(1):558–561. https://doi.org/10.1103/PhysRevB.47.558
36. Kresse G, Hafner J (1994) Ab initio molecular-dynamics simulation of the liquid-metal–amorphous-semiconductor transition in germanium. Phys Rev B 49(20):14251–14269. https://doi.org/10.1103/PhysRevB.49.14251
37. Kresse G, Furthmüller J (1996) Efficient iterative schemes for ab initio total-energy calculations using a plane-wave basis set. Phys Rev B 54(16):11169–11186. https://doi.org/10.1103/PhysRevB.54.11169

38. Kresse G, Furthmüller J (1996) Efficiency of ab-initio total energy calculations for metals and semiconductors using a plane-wave basis set. Comput Mater Sci 6(1):15–50. https://doi.org/10.1016/0927-0256(96)00008-0
39. Perdew JP, Burke K, Ernzerhof M (1996) Generalized gradient approximation made simple. Phys Rev Lett 77(18):3865–3868. https://doi.org/10.1103/PhysRevLett.77.3865
40. Lee K, Murray ÉD, Kong L, Lundqvist BI, Langreth DC (2010) Higher-Accuracy Van der Waals density functional. Phys Rev B 82(8):081101. https://doi.org/10.1103/PhysRevB.82.081101
41. Kresse G, Hafner J (1994) Norm-conserving and ultrasoft pseudopotentials for first-row and transition elements. J Phys Condens Matter 6(40):8245–8257. https://doi.org/10.1088/0953-8984/6/40/015
42. Kresse G, Joubert D (1999) From ultrasoft pseudopotentials to the projector augmented-wave method. Phys Rev B 59(3):1758–1775. https://doi.org/10.1103/PhysRevB.59.1758
43. Wheeler DP (1925) Precision measurements of the lattice constants of twelve common metals. Phys Rev 25(6):753–761. https://doi.org/10.1103/PhysRev.25.753
44. Gražulis S, Chateigner D, Downs RT, Yokochi AFT, Quirós M, Lutterotti L, Manakova E, Butkus J, Moeck P, Le Bail A (2009) Crystallography open Database – an open-Access collection of crystal structures. J Appl Crystallogr 42(4):726–729. https://doi.org/10.1107/S0021889809016690
45. Luque A (2024) accessed Aug 27, BOLOS: An open source solver for the Boltzmann equation https://github.com/aluque/bolos
46. Hagelaar GJM, Pitchford LC (2005) Solving the Boltzmann equation to obtain electron transport coefficients and rate coefficients for fluid models. Plasma Sources Sci Technol 14(4):722–733. https://doi.org/10.1088/0963-0252/14/4/011
47. Wanten B, Vertongen R, De Meyer R, Bogaerts A, Plasma-Based (2023) CO_2 conversion: how to correctly analyze the performance?? J Energy Chem 86:180–196. https://doi.org/10.1016/j.jechem.2023.07.005
48. Slaets J, Loenders B, Bogaerts A (2024) Plasma-Based Dry Reforming of CH_4: Plasma Effects vs. Thermal Conversion. *Fuel 360* (September 2023), 130650. https://doi.org/10.1016/j.fuel.2023.130650
49. Slaets J, Morais E, Bogaerts A (2025) Afterglow quenching in plasma-based dry reforming of methane: a detailed analysis of the post-plasma chemistry via kinetic modelling. RSC Sustain 3(3):1477–1493. https://doi.org/10.1039/d4su00676c
50. Afonso J, Vialetto L, Guerra V, Viegas P (2024) Plasma-Induced reversible surface modification and its impact on oxygen heterogeneous recombination. J Phys D: Appl Phys 57(4):04LT01. https://doi.org/10.1088/1361-6463/ad039b
51. Viegas P, Silveira J, Cunha Dias T, Guaitella O, Sofia M, Candás A, Guerra V (2024) Surface recombination in pyrex in oxygen DC glow discharges: mesoscopic modelling and comparison with experiments. Plasma Sources Sci Technol 33(5):055003. https://doi.org/10.1088/1361-6595/ad4055
52. Booth JP, Guaitella O, Chatterjee A, Drag C, Guerra V, Lopaev D, Zyryanov S, Rakhimova T, Voloshin D, Mankelevich Y (2019) Oxygen (^{3}P) atom recombination on a pyrex surface in an O_2 plasma. Plasma Sources Sci Technol 28(5):055005. https://doi.org/10.1088/1361-6595/ab13e8
53. Neyts EC, Ostrikov KK, Sunkara MK, Bogaerts A (2015) Plasma catalysis: synergistic effects at the nanoscale. Chem Rev 115(24):13408–13446. https://doi.org/10.1021/acs.chemrev.5b00362
54. Ibach H, Erley W, Wagner H (1980) The preexponential factor in desorption — CO on Ni(111). Surf Sci 92(1):29–42. https://doi.org/10.1016/0039-6028(80)90240-X
55. Kim YC, Boudart M (1991) Recombination of O, N, and H Atoms on Silica: Kinetics and Mechanism. *Langmuir 7* (12), 2999–3005. https://doi.org/10.1021/la00060a016
56. Afonina NE, Gromov VG, Kovalev VL (2000) Modeling of the catalytic properties of high-temperature surface insulation in a dissociated carbon dioxide — nitrogen mixture. Fluid Dyn 35(1):87–94. https://doi.org/10.1007/BF02698792
57. Larsen AH, Mortensen JJ, Blomqvist J, Castelli IE, Christensen R, Dułak M, Friis J, Groves MN, Hammer B, Hargus C, Hermes ED, Jennings PC, Jensen PB, Kermode J, Kitchin JR, Kolsbjerg EL, Kubal J, Kaasbjerg K, Lysgaard S, Bergmann Maronsson J, Maxson T, Olsen T, Pastewka L, Peterson A, Rostgaard C, Schiøtz J, Schütt O, Strange M, Thygesen KS, Vegge T, Vilhelmsen L, Walter M, Zeng Z, Jacobsen KW (2017) The atomic simulation Environment—a python library for working with atoms. J Phys Condens Matter 29(27):273002. https://doi.org/10.1088/1361-648X/aa680e
58. Chung Y, Green WH (2025) New modified arrhenius equation to describe the temperature dependence of liquid phase reaction rates. Chem Eng J 516:163300. https://doi.org/10.1016/j.cej.2025.163300
59. Modified Arrhenius Equation. In The IUPAC Compendium of Chemical Terminology; International Union of Pure and Applied Chemistry (IUPAC): Research Triangle Park, NC (2014) https://doi.org/10.1351/goldbook.M03963
60. Michiels R, Gerrits N, Neyts E, Bogaerts A (2024) Plasma catalysis modeling: how ideal is atomic hydrogen for Eley–Rideal? J Phys Chem C 128(27):11196–11209. https://doi.org/10.1021/acs.jpcc.4c02193

61. Carrasco E, Jiménez-Redondo M, Tanarro I, Herrero VJ (2011) Neutral and ion chemistry in low pressure Dc plasmas of H_2/N_2 mixtures: routes for the efficient production of NH_3 and NH_4^+. Phys Chem Chem Phys 13(43):19561–19572. https://doi.org/10.1039/c1cp22284h
62. Chen Z, Koel BE, Sundaresan S (2022) Plasma-Assisted catalysis for ammonia synthesis in a dielectric barrier discharge reactor: key surface reaction steps and potential causes of low energy yield. J Phys D: Appl Phys 55(5):055202. https://doi.org/10.1088/1361-6463/ac2f12
63. Hong J, Pancheshnyi S, Tam E, Lowke JJ, Prawer S, Murphy AB (2017) Kinetic modelling of NH_3 production in N_2–H_2 Non-Equilibrium Atmospheric-Pressure plasma catalysis. J Phys D: Appl Phys 50(15):154005. https://doi.org/10.1088/1361-6463/aa6229
64. Jiménez-Redondo M, Chatain A, Guaitella O, Cernogora G, Carrasco N, Alves LL, Marques L (2020) N_2 –H_2 capacitively coupled Radio-Frequency discharges at low pressure: II. Modeling results: the relevance of Plasma-Surface interaction. Plasma Sources Sci Technol 29(8):085023. https://doi.org/10.1088/1361-6595/ab9b1b
65. van 't Veer K, Engelmann Y, Reniers F, Bogaerts A (2020) Plasma-Catalytic ammonia synthesis in a DBD plasma: role of microdischarges and their afterglows. J Phys Chem C 124(42):22871–22883. https://doi.org/10.1021/acs.jpcc.0c05110
66. Gorbanev Y, Engelmann Y, van't Veer K, Vlasov E, Ndayirinde C, Yi Y, Bals S, Bogaerts A (2021) Al_2O_3-supported transition metals for plasma-catalytic NH_3 synthesis in a DBD plasma: metal activity and insights into mechanisms. Catalysts 11(10):1230. https://doi.org/10.3390/catal11101230
67. Melin GA, Madix RJ (1971) Energy accommodation during oxygen atom recombination on metal surfaces. Trans Faraday Soc 67:198–211. https://doi.org/10.1039/tf9716700198
68. Cauquot P, Cavadias S, Amouroux J (1998) Thermal energy accommodation from oxygen atoms recombination on metallic surfaces. J Thermophys Heat Transf 12(2):206–213. https://doi.org/10.2514/2.6323
69. Greaves JC, Linnett JW (1958) The recombination of oxygen atoms at surfaces. Trans Faraday Soc 54:1323–1330. https://doi.org/10.1039/tf9585401323
70. May JW, Linnett JW (1967) Recombination of atoms at surfaces. An effusion method applied to oxygen atom recombination. J Catal 7(4):324–341. https://doi.org/10.1016/0021-9517(67)90161-3
71. Chantry PJ (1987) A simple formula for diffusion calculations involving wall reflection and low density. J Appl Phys 62(4):1141–1148. https://doi.org/10.1063/1.339662
72. Morillo-Candas AS, Drag C, Booth J-P, Dias TC, Guerra V, Guaitella O (2019) Oxygen atom kinetics in CO_2 plasmas ignited in a DC glow discharge. Plasma Sources Sci Technol 28(7):075010. https://doi.org/10.1088/1361-6595/ab2b84
73. Mehio N, Dai S, Jiang DE (2014) Quantum mechanical basis for kinetic diameters of small gaseous molecules. J Phys Chem A 118(6):1150–1154. https://doi.org/10.1021/jp412588f
74. Viegas P, Dias TC, Fromentin C, Chukalovsky A, Mankelevich Y, Proshina O, Rakhimova T, Guerra V, Voloshin D (2023) Comparison between 1D radial and 0D global models for Low-Pressure oxygen DC glow discharges. Plasma Sources Sci Technol 32(2):024002. https://doi.org/10.1088/1361-6595/acbb9c
75. Fridman A (2008) Plasma chemistry. Cambridge University Press, New York
76. Gerrits N, Bogaerts A Vibrationally excited Molecule-Metal surface reactions in heterogeneous and plasma catalysis: going beyond the Fridman-Macheret α model. *EES Catal*. Submitted
77. Polanyi JC (1972) Concepts in reaction dynamics. Acc Chem Res 5:161–168
78. Yin R, Guo H (2024) Multidimensional dynamics of CO_2 dissociative chemisorption on Cu(110). J Phys Chem C 128(23):9483–9491. https://doi.org/10.1021/acs.jpcc.4c00850
79. Booth J-P, Chatterjee A, Guaitella O, Sousa JS, Lopaev D, Zyryanov S, Rakhimova T, Voloshin D, Mankelevich Y, de Oliveira N, Nahon L (2020) Determination of absolute O(3 P) and O 2 (a 1 Δ g) densities and kinetics in fully modulated O 2 Dc glow discharges from the O 2 (X 3 Σ g –) afterglow recovery dynamics. Plasma Sources Sci Technol 29(11):115009. https://doi.org/10.1088/1361-6595/abb5e7
80. Wu C, Schmidt DJ, Wolverton C, Schneider WF (2012) Accurate coverage-dependence incorporated into first-principles kinetic models: catalytic NO oxidation on Pt (111). J Catal 286(2):88–94. https://doi.org/10.1016/j.jcat.2011.10.020
81. Hoffmann MJ, Medford AJ, Bligaard T (2016) Framework for scalable adsorbate–adsorbate interaction models. J Phys Chem C 120(24):13087–13094. https://doi.org/10.1021/acs.jpcc.6b03375
82. Grabow LC, Hvolbæk B, Nørskov JK (2010) Understanding trends in catalytic activity: the effect of adsorbate–adsorbate interactions for CO oxidation over transition metals. Top Catal 53(5–6):298–310. https://doi.org/10.1007/s11244-010-9455-2
83. Montemore MM, van Spronsen MA, Madix RJ, Friend CM (2018) O2 activation by metal surfaces: implications for bonding and reactivity on heterogeneous catalysts. Chem Rev 118(5):2816–2862. https://doi.org/10.1021/acs.chemrev.7b00217
84. Rond C, Bultel A, Boubert P, Chéron BG (2008) Spectroscopic measurements of nonequilibrium CO_2 plasma in RF torch. Chem Phys 354(1–3):16–26. https://doi.org/10.1016/j.chemphys.2008.09.006

85. Falsig H, Hvolbæk B, Kristensen IS, Jiang T, Bligaard T, Christensen CH, Nørskov JK (2008) Trends in the catalytic CO oxidation activity of nanoparticles. Angew Chem Int Ed 47(26):4835–4839. https://doi.org/10.1002/anie.200801479
86. Kummer JT (1986) Use of noble metals in automobile exhaust catalysts. J Phys Chem 90(20):4747–4752. https://doi.org/10.1021/j100411a008
87. Vojvodic A, Nørskov JK (2015) New design paradigm for heterogeneous catalysts. Natl Sci Rev 2(2):140–143. https://doi.org/10.1093/nsr/nwv023
88. Evans MG, Polanyi M (1938) Inertia and driving force of chemical reactions. Trans Faraday Soc 34:11–24. https://doi.org/10.1039/tf9383400011